

1 **Multi-year black carbon observations and modeling close to the**  
2 **largest gas flaring and wildfire regions (Western Siberian Arctic)**

3 **Olga B. Popovicheva<sup>1</sup>, Marina A. Chichaeva<sup>2</sup>, Nikolaos Evangeliou<sup>3,\*</sup>, Sabine Eckhardt<sup>3</sup>,**  
4 **Evangelia Diapouli<sup>4</sup>, and Nikolay S. Kasimov<sup>2</sup>**

5  
6 <sup>1</sup>SINP, Lomonosov Moscow State University, 119991 Moscow, Russia

7 <sup>2</sup>Faculty of Geography, Lomonosov Moscow State University, 119991 Moscow, Russia

8 <sup>3</sup>NILU, Department for Atmospheric & Climate Research (ATMOS), 2007 Kjeller, Norway

9 <sup>4</sup>ERL, Institute of Nuclear and Radiological Science & Technology, Energy & Safety, NCSR  
10 Demokritos, 15341 Attiki, Athens, Greece

11 \* Corresponding author: N. Evangeliou ([Nikolaos.Evangeliou@nilu.no](mailto:Nikolaos.Evangeliou@nilu.no))

12

13

14 **Abstract**

15 The influence of aerosols on the Arctic system remains associated with significant  
16 uncertainties, particularly concerning black carbon (BC). The polar aerosol station "Island Bely"  
17 (IBS), located in Western Siberian Arctic, was established to enhance aerosol monitoring.  
18 Continuous measurements from 2019 to 2022 revealed the long-term effects of light-absorbing  
19 carbon. During the cold period, the annual average light absorption coefficient was  $0.7 \pm 0.7 \text{ Mm}^{-1}$ ,  
20 decreasing by 2-3 times during the warm period. The interannual mean showed a peak in February  
21 ( $0.9 \pm 0.8 \text{ Mm}^{-1}$ ), a ten times lower minimum in June, and exhibited high variability in August ( $0.7$   
22  $\pm 2.2 \text{ Mm}^{-1}$ ). An increase of up to 1.5 at shorter wavelengths from April to September suggests  
23 contribution from brown carbon (BrC). The annual mean equivalent black carbon (*eBC*)  
24 demonstrated considerable interannual variability, with the lowest in 2020 ( $24 \pm 29 \text{ ng m}^{-3}$ ).  
25 Significant difference was observed between Arctic Haze and Siberian wildfire periods, with  
26 record-high pollution levels in February 2022 ( $110 \pm 70 \text{ ng m}^{-3}$ ) and August 2021 ( $83 \pm 249 \text{ ng}$   
27  $\text{m}^{-3}$ ). Anthropogenic BC contributed 83% to the total for the entire study period and gas flaring,  
28 domestic combustion, transportation, and industrial emissions dominated. During the cold season,  
29 >90% of surface BC was attributed to anthropogenic sources, mainly gas flaring. In contrast, during  
30 the warm period, Siberian wildfires contributed to BC concentrations by 48%. In August 2021,  
31 intense smoke from Yakutian wildfires was transported at high altitudes during the region's worst  
32 fire season in 40 years.

Deleted: on Bely Island (

Deleted: Kara Sea) in the

Deleted: in the Arctic

Deleted: in-situ

Deleted: approximately

Deleted: The absorption Ångström exponent (*AAE*) indicated presence of mixed and aged BC. ...

Deleted: light absorbing

Deleted: Overall, a

Deleted: Notably, unprecedented smoke was transported from Yakutian wildfires at high altitudes in August 2021, marking the most severe fire season in the region over the past four decades....

## 48 1 Introduction

49 Multiple socio-economic drivers and feedbacks, including air pollution (Arnold et al., 2016)  
50 influence the natural and human environment of the Arctic. Over the last few decades, the Arctic  
51 warms more than three times faster than the global average (AMAP, 2021). The pronounced rapid  
52 changes affect atmospheric transport and aerosol relative source contributions (Heslin-Rees et al.,  
53 2020). Drier conditions and warmer temperatures are the main cause of enhanced fire activity.  
54 Boreal forest fires become more frequent and severe (Rogers et al., 2020), especially in Central  
55 Siberia, and Northern America (Kasischke and Turetsky, 2006; Kharuk and Ponomarev, 2017;  
56 Veraverbeke et al., 2017). Widespread smoke plumes, particularly in Siberia, lead to substantial  
57 deterioration of air quality increasing fine particulate matter (Silver et al., 2024).

58 Interactions between aerosol and different cloud types, available solar radiation, sea ice,  
59 surface albedo, Arctic and lower latitude removal processes, and atmospheric transport patterns.  
60 affect Arctic pollution and its climate impacts (Willis et al., 2018), such as the Arctic haze (namely  
61 the persistent Arctic air pollution during late winter and early spring). To understand such  
62 phenomena and thus reduce their impact, there is a clear need for comprehensive studies of the  
63 climate-relevant aerosol processes that occur in the Arctic. A species of major concern is BC, a  
64 short-lived climate forcer (Schmale et al., 2021). BC is emitted from the incomplete combustion of  
65 fossil fuel and biomass; it is defined as the portion of carbonaceous aerosols, which absorb strongly  
66 in the entire climate relevant wavelength region of the solar spectrum (i.e. IR-VIS-UV). BC  
67 contributes to Arctic warming in multiple ways (e.g., Lee et al., 2013), including the darkening  
68 effect of BC deposited on snow and ice (Flanner, 2013). AMAP (2015) reports that the Arctic  
69 equilibrium temperature response is (+0.4°C) due to forcing from atmospheric BC and (+0.22°C)  
70 due to snow BC.

71 At present, the largest uncertainties when assessing aerosol impact on the climate are  
72 attributed to BC (AMAP, 2021). To follow-up on this, BC measurements are taken at various polar  
73 regions in the European, Siberian, and Canadian Arctic (Stone et al., 2014; Yttri et al., 2014;  
74 Popovicheva et al., 2019a; Winiger et al., 2019; Manousakas et al., 2020; Gilardoni et al., 2023).  
75 For instance, Stathopoulos et al. (2021) reported on the long-term impact of light-absorbing carbon  
76 in the high Arctic by analysing 15 years of data from the Zeppelin station (Svalbard), while  
77 Schmale et al. (2022) studied the status of the Arctic haze peak concentrations at 10 Arctic  
78 observatories.

79 There is a large diversity in magnitude and variability of aerosol optical properties, reflecting  
80 differences in sources throughout the Arctic (Schmeisser et al., 2018). BC measurements are based  
81 on various instrumentations and methods that increase uncertainty (Sharma et al., 2017; Asmi et al.,

2021; Ohata et al., 2021). The optical properties of BC have been previously evaluated against direct mass measurements techniques (Sharma et al., 2004; Eleftheriadis et al., 2009; Yttri et al., 2024). The conversion of light attenuation to absorbing carbon mass concentration is performed by the mass-specific absorption coefficient (*MAC*) (Petzold et al., 2013) that is highly influenced by the aerosol mixing state and non-BC light-absorbing species such as organic matter and mineral dust (Zanatta et al., 2018) and varies in time and space depending on sources and transformations during transport (Bond et al., 2013; Chen et al., 2023). Therefore, it is crucial to quantify the contribution of non-BC component and aging in order to determine the actual *MAC* value experimentally at each site (Singh et al., 2024).

The *AAE* defined as the relative fraction of wavelength - dependence of absorption of BC versus other light absorbing constituents, also differs from site to site (Schmeisser et al., 2018). A fraction of organic aerosol, the BrC, increases the aerosol absorbing properties at short UV-VIS wavelengths (Sandradewi et al., 2008; Grange et al., 2020; Helin et al., 2021) and dominates the absorption during wildfire seasons (Bali et al., 2024). BrC originates mainly from biomass burning (BB) and can impose strong warming effect in the Arctic, especially in the summertime (Yue et al., 2022).

Despite its remoteness, the Arctic is one of the main receptors of anthropogenic air pollutant emissions from the Northern Hemisphere (Stohl et al., 2013). BC trends and seasonality at three Arctic sites, Alert (Canadian Arctic), Barrow/Utqiagvik (American Arctic), and Zeppelin, Ny-Ålesund (European Arctic) reveal a negative trend of 40% over 16 years due to the anthropogenic emission reduction (Sharma et al., 2013). The recent increase in fires and their earlier starts, due to the ongoing warming, have made wildfires in the Northern Eurasia a significant source of Arctic BC (Evangelou et al., 2016). Fossil fuel combustion is the major source of BC in the Arctic troposphere (50–94%) (55–68% at the surface and 58–69% in the snow) and BB dominates at certain altitudes (600–800 hPa) between April to September (Qi and Wang, 2019). This agrees with Matsui et al. (2022) who reported that the largest contribution to Arctic BC is from BB sources in Siberia travelling at high altitudes.

Northern Eurasia, particularly Siberia, is a key source region of pollution in the Arctic. Source quantification (Zhu et al., 2020) shows that surface Arctic BC originates mainly from anthropogenic emissions in Russia (56%). The reason for this is that the largest oil and gas producing facilities of Western Siberia are located along the main pathway of air masses that enter the Arctic and thus have a disproportionally large contribution to the Arctic lower troposphere (Stohl, 2006; Stohl et al., 2013). Eleftheriadis et al. (2009) and Tunved et al. (2013) identified these regions as a key source for the highest measured BC in the European Arctic. The impact of long-range transport from these



regions has been previously reported in Ice Cape Baranova station (Manousakas et al., 2020) and Tiksi (Northeastern Siberia) (Winiger et al., 2017; Popovicheva et al., 2019a). Airborne observations over the coast of the Arctic seas have identified the long-term transport of the industrial pollution (Zenkova et al., 2022). Furthermore, efforts have sought to develop BC emission inventories for the Siberian Arctic, based on activity data from local information, improved gas flaring emissions, and satellite data (Huang et al., 2015; Böttcher et al., 2021; Kostykin et al., 2021; Vinogradova and Ivanova, 2023). To better quantify the source contribution to the Arctic environment, targeted aerosol measurements close to the flaring facilities are needed. The present operating Eurasian Arctic stations are all too far away to allow assessing how air masses are affected by different source categories (Stohl et al., 2013). However, ship campaigns focusing on BC close to main source regions (e.g., gas flaring facilities of the Western Siberia) have provided a better constraint of how anthropogenic and BB sources influence Arctic pollution (Popovicheva et al., 2017b).

Another major source of the Arctic BC is wildfires in the Siberian and Far Eastern regions, which have grown in recent summers (Bondur et al., 2020). Airborne observations of BC in Siberia have confirmed impact forest fires (Paris et al., 2009). Eastern Siberia (Yakutia) has been prone to large wildfires due to a combination of hot summers ( $> 40^{\circ}\text{C}$ ) and low humidity (Tomshin and Solovyevev, 2022). For instance, wildfires in summer 2019 in Eastern Siberia occurred along the trans-Arctic transport pathway resulting in enhanced aerosol load observed in Western Canada (Johnson et al., 2021). BB emissions occurring at midlatitudes reached the European Arctic in 2020 influencing aerosol composition (Gramlich et al., 2024).

Despite the necessity for detailed observations in the Northwestern Siberia, a dense observational network is still absent. Towards this, the polar aerosol station on the Bely Island (Kara Sea, Western Siberia) started to operate in August 2019 (Popovicheva et al., 2022, 2023). The significance of high-quality measurements at the IBS is documented, as the station is located along the main pathway of large-scale emission plumes from industrial regions and Siberian wildfires entering the Arctic (Popovicheva et al., 2022). Further investigation performed at IBS in August 2021 showed impact from a long-range transport event with unprecedented high concentrations of carbonaceous aerosol (Schneider et al., 2024).

In this paper, we show improved light absorption long-term measurements and BC seasonal and inter-annual variability in the Western Siberian Arctic from three and a half years (2019-2022) of observations at IBS. BC was calculated in two ways: as *eBC* by an aethalometer and as elemental carbon (EC) by thermal-optical analysis. We further evaluate the seasonal changes in the observed absorption coefficients. Seasonal difference in intensive optical properties is shown by the

150 wavelength-dependent *AAE*, which acts as indication of the BrC impact. Estimated site-specific  
151 absorption coefficient (*SAC*) considered the specific seasonal effects of mixing and aging of  
152 aerosols at IBS. We further assess the inter-annual variability of origin, transport and main BC  
153 sources using modelling tools coupled with the most recent anthropogenic and BB emission  
154 datasets.

155 **2 Methods**

156 **2.1 Polar aerosol Island Bely station, location and meteorology**

157 The aerosol IBS of Moscow State University (73020'7.57"N, 70040'49.05"E) is shown in  
158 [Figure 1a](#) together with other Polar Arctic observatories. Western Siberia is the world's largest gas  
159 flaring region with a leading oil and gas production industry ([Figure 1b](#)). It is also an area under  
160 intensive exposure by Siberian wildfires (Tomshin and Solovyev, 2022; Voronova et al., 2022). A  
161 satellite image of smoke plume for 5<sup>th</sup> August 2021 was obtained from  
162 <https://worldview.earthdata.nasa.gov>. Fires are shown from the Fire Information for Resource  
163 Management System (FIRMS) (<https://firms.modaps.eosdis.nasa.gov/map>) ten days back in time.

164 The climate at IBS is characterized by a large annual variability determined by alternating  
165 periods of the polar night and midnight sun. Basic meteorological parameters, such as temperature,  
166 wind speed and direction were obtained every 3 hours from a meteorological station located 500 m  
167 away from the IBS. The cycles of temperature, precipitation, snow coverage, wind speed and  
168 relative humidity are shown in [Figure S 1](#). Annual temperature varied from -39°C to 23°C (mean: -  
169 6±12°C) ([Table S 1](#)). For further analysis, we have split the annual cycle in two periods based on  
170 the prevailing temperatures, November-April (“cold period”, -15.9±9.1) and May - October (“warm  
171 period”, 2.8±5.8). High relative humidity of 87±8% was typical for the study period, with less than  
172 80% observed in winter 2020. Precipitation was maximum in summer (22 mm) with constant snow  
173 coverage from October to May. Wind was relatively stable, with a mean speed of 6±3 m s<sup>-1</sup>, which  
174 increased in winter up to 17 m s<sup>-1</sup> ([Figure S 1](#)).

175 Wind patterns for the cold period in [Figure S 1](#), show a prevailing wind direction from south,  
176 southwest, and southeast. Winds were predominantly continental, rarely occurring from the ocean;  
177 significant emission sources from the continent were downwind. In the warm period, the wind  
178 patterns were more spatially homogeneous with northeastern direction. Period from June and  
179 September was characterized by a frequent occurrence of oceanic air masses and constant wind  
180 speeds.

Deleted: Figure 1

Deleted: Figure 1

Deleted: Figure S 1

Deleted: Table S 1

Deleted: Figure S 1

Deleted: Figure S 1

Deleted: takes place

## 2.2 Aerosol optical and chemical characterization

The aerosol pavilion is situated approximately half a km to the southeast of the meteorological station. An aerosol sampling system composed from three total suspended particle inlets has been installed approximately 1.5 m above the roof and 4 m above the ground. They are equipped with an electric heating wire to prevent rimming and ice blocking of the system. One inlet was used for the real-time light-absorption measurements with air flow 5 L min<sup>-1</sup>. Two other inlets low-volume samplers (Derenda, Germany) were used for sampling of total suspended particles (TSP) operating at 2.3 m<sup>3</sup> h<sup>-1</sup> flow (0°C, 1013.25 hPa).

An Aethalometer model AE33 (Magee Scientific, Aerosol d.o.o.) was used to measure the light attenuation caused by particles deposited on two filter spots at different flow rates (Drinovec et al., 2015) and at seven wavelengths from ultraviolet (370 nm) to infrared (950 nm). The “dual spot” technique is applied for real-time loading effect compensation. Optical absorption of aerosols on the filter is influenced by scattering of light within the filter; the enhancement of optical absorption is described by the factor C that depends on the filter material. The producer recommends an enhancement factor of 1.57 for TFE-coated glass fiber filter. The light-absorbing content of carbonaceous aerosol is reported as *eBC* concentration by aethalometer (*eBC<sub>AET</sub>*) for the given wavelength  $\lambda$ , which is determined for each time interval from the change in the light absorption using the *MAC*. The aerosol optical absorption coefficient (*b<sub>abs</sub>*) is therefore:

$$b_{abs}(\lambda) = eBC_{AET}(\lambda) \times MAC(\lambda) \quad (1)$$

where *eBC<sub>AET</sub>* at 880 nm is determined using the *MAC* of 7.7 m<sup>2</sup> g<sup>-1</sup>. The aerosol optical absorption coefficient for different wavelengths is determined with their *MAC* values that are equal to 11.58, and 13.14 m<sup>2</sup> g<sup>-1</sup> at 590, and 520 nm, respectively.

To represent the spectral dependence of the light absorption, the *AAE* was derived by using a fitted power law relationship:

$$b_{abs}(\lambda) = b_{abs}(\lambda_o) \times \left(\frac{\lambda}{\lambda_o}\right)^{-AAE} \quad (2)$$

where *b<sub>abs</sub>*( $\lambda_o$ ) is the absorption coefficient at the reference wavelength  $\lambda_o$ , *AAE* is a measure of strength of the spectral variation of aerosol light absorption.

BC absorbs strongly in the NIR-VIS (near-infrared and visible) with only moderate increment towards the shorter wavelengths. Light absorbing organic components related to BrC absorb light at shorter wavelengths more effectively than at 880 nm, which is observed as an increased *AAE* (Sandradewi et al., 2008; Grange et al., 2020; Helin et al., 2021). The total light absorption is assumed to include the contribution of both BC and BrC (Ivančić et al., 2022):

$$b_{abs}(\lambda) = b_{abs/BC}(\lambda) + b_{abs/BrC}(\lambda) \quad (3)$$

Using Eq. 1, the BrC absorption becomes:  $b_{abs/BrC}(\lambda) = b_{abs}(\lambda) - b_{abs}(\lambda_0) \times \left(\frac{\lambda}{\lambda_0}\right)^{-AAE}$  (4)

Light-absorption measurements were performed for three and a half years, from 10 August 2019 to 31 December 2022, with a time resolution of 1 min. Data were cleaned based on analysis of meteorological parameters by examining whether the wind originated from the direction of the meteorological station where diesel generators operated. In such cases, strong peaks of BC were removed from further analysis. Around 6.4 % of the hourly-average data were cleaned from the dataset due to local pollution impact. To avoid the instrumental noise when calculating the *AAE*, the z-score was used that calculates the ratio of difference between a single raw data value and the data mean to the data standard deviation. Outliers (< -3 and > 3 of observation's z-score) were removed from the dataset.

A thermal EC analysis was conducted for the samples in parallel to AE33. Sampling was performed on 47 mm quartz fiber (Pallflex) filters preheated at 600°C for 5 h. The low concentrations of ambient aerosols necessitate that the sampling times reach up to a week, in order to allow the filter loading to exceed the detection limit for relevant aerosol chemistry analyses. The total number of samples limited by the low detection limit of the thermal-optical instrument were 180.

Organic (OC) and EC were measured by thermo-optical transmittance (TOT) analysis (Lab OC-EC Aerosol Analyzer, Sunset Laboratory, Inc.) using the methodology reported in Popovicheva et al. (2019) and Manousakas et al. (2020). Quartz filter samples were heated first up to 650 °C in He atmosphere and then up to 850 °C in a mixture of 2% O<sub>2</sub> in He, using the controlled heating ramps of the EUSAAR\_2 thermal protocol. OC evolves in inert atmosphere, while the thermal refractory fraction EC is oxidized in the He-O<sub>2</sub> atmosphere. Charring correction due to pyrolytic carbon was applied by monitoring the sample transmittance throughout the heating process. The limit of detection for the EC analysis was 0.05 µg C cm<sup>-2</sup>. QA/QC procedures of EN 16909:2017 were also applied during TOT analysis. Laboratory and field blanks were prepared and ran following the same analytical procedures as for the samples.

Both methods have important uncertainties (10 - 80%, Sharma et al., 2017; Ohata et al., 2021). The determination of EC by thermo-optical analysis may be impacted by the presence of carbonate carbon (CC), which is quantified during analysis as OC and/or EC. The contribution of CC in fine aerosol is generally considered negligible but its interference may be significant for coarse aerosol and samples heavily impacted by resuspended soil. The split between EC and OC

may be also affected by the presence of light-absorbing species others than EC, such as light absorbing organic carbon. In addition, the presence of mineral oxides, such as iron oxide, might provide oxygen during analysis and lead to pre-oxidation of EC in inert atmosphere. *eBC* might overestimate BC if there are coexisting components such as BrC (Chakrabarty et al., 2010) and dust (Petzold et al., 2009). In addition, the aethalometer response depends on filter loading and multiple scattering by the filter medium and sampled aerosol particles (Backman et al., 2017).

Validations of *eBC* retrievals were performed against results from thermal-optical analysis of EC according to an approach that has been used previously in Sharma et al. (2004), Eleftheriadis et al. (2009) and Yttri et al. (2014). To convert optical absorption at 880 nm to BC mass, the *SAC* was estimated as:

$$SAC = \frac{b_{abs/BC}}{EC} \quad (5)$$

Data processing was performed using Deming's total least-squares regression to compare measurements from different methods and modelling, estimate the *MAC*, and evaluate correlations among variables (R package "Deming"; (Therneau, 2024)). Deming regression fits a couple of variables considering the independent errors of both. The errors are assumed to be normally distributed; the error ratio is 1, and the regression results are equivalent to the orthogonal regression with the intercept forced through zero.

### 2.3 Atmospheric dispersion modelling and emission inventories

To investigate the air mass transport and possible origin of BC during the study period (2019 – 2023), the Lagrangian particle dispersion model FLEXPART version 10.4 was used (Pisso et al., 2019) driven by hourly reanalysis meteorological fields (ERA5) from the European Centre for Medium-Range Weather Forecasts (ECMWF) with 137 vertical levels (up to approximately 80 km) and a horizontal resolution of 0.5°×0.5° (Hersbach et al., 2020). In FLEXPART, computational particles were released at heights 0 - 100 m from the receptor (IBS) and tracked backward in time in FLEXPART's "retroplume" mode. Simulations extended over 30 days backward in time, sufficient to include most BC emissions arriving at the station, given a typical BC lifetime of 1 week (Bond et al., 2013). The tracking includes gravitational settling for spherical particles, dry and wet deposition of aerosols (Grythe et al., 2017), turbulence (Cassiani et al., 2015), unresolved mesoscale motions (Stohl et al., 2005), and deep convection (Forster et al., 2007). The FLEXPART output consists of a footprint emission sensitivity that expresses the probability of any emission occurring in each grid-cell to reach the receptor. The footprint can be converted to modelled concentration at the receptor, when coupled with gridded emissions from an emission inventory. Modelled concentrations can be calculated as a function of the time elapsed since the emission has occurred (i.e., "age"), which can

285 be shown as “age spectrum”, while masks of specific regions/continents can give the continental  
286 contribution to the simulated concentration (i.e., “continent spectrum”).

287 The source contribution to receptor BC is calculated by combining each gridded emission  
288 sector (e.g. gas flaring, transportation, waste management etc...) from an emission inventory with  
289 the footprint emission sensitivity (as described in the previous paragraph). Calculations for  
290 anthropogenic sources (emission sectors are described below) and open BB were performed  
291 separately. This enabled identification of the exact origin of BC and allowed for quantification of its  
292 source contribution. Anthropogenic emissions were adopted from the latest version (v6b) of the  
293 ECLIPSE (Evaluating the CLimate and Air Quality ImPacts of ShortlivEd Pollutants) dataset, an  
294 upgraded version of the previous version (Klimont et al., 2017). The inventory includes emissions  
295 from industrial combustion (IND), from the energy production sector (ENE), residential and  
296 commercial emissions (DOM), emissions from waste treatment and disposal sector (WST),  
297 transportation (TRA), shipping activities (SHP) and gas flaring emissions (FLR). The methodology  
298 for obtaining emissions from FLR specifically over the Russian territories has been improved in  
299 ECLIPSEv6 (Böttcher et al., 2021). Annual total and monthly anthropogenic emissions are shown  
300 in [Figure S 2](#), BB was adopted from the Copernicus Global Fire Assimilated System (CAMS  
301 GFAS) (Kaiser et al., 2012) because this product provides an estimation of the injection altitude of  
302 the fire emissions that is crucial for accurate simulation of the BB dispersion. Annual total and daily  
303 fire emissions from CAMS GFAS are shown in [Figure S 3](#).

Deleted: Figure S 2

Deleted: Figure S 3

## 304 3 Results

### 305 3.1 Aerosol light-absorption

306 Light-absorption coefficients at 880 nm,  $b_{abs}(880)$  were used to infer  $eBC$  mass  
307 concentrations.  $b_{abs}(880)$  were plotted as hourly and monthly means during the entire study period  
308 (2019-2022) ([Figure 2](#)). [Table 1](#) presents the data statistical summary. The mean  $\pm$  sigma (median)  
309 value of  $b_{abs}(880)$  was  $0.5 \pm 0.9$  (0.27)  $Mm^{-1}$  for the entire study period. In the cold period the  
310 annual average mean (median) of  $b_{abs}(880)$  was  $0.7 \pm 0.7$   $Mm^{-1}$  (0.5), during the warm period it  
311 was 1.9 (2.5) times less. There is a clear seasonality consistent with the Arctic aerosol light  
312 absorption from other studies (Stathopoulos et al., 2021; Schmale et al., 2022; Pulimeno et al.,  
313 2024) due to the formation of the polar dome and the slow removal processes in the Arctic in winter  
314 (Law and Stohl, 2007). 15 years (2001-2015) record at Zeppelin demonstrated that the long-term  
315 seasonality of light absorbing carbon (Stathopoulos et al., 2021)  $b_{abs}(880)$  was  $0.112 Mm^{-1}$

Deleted: Figure 2

Deleted: Table 1

320 (median) in the cold period and  $0.035 \text{ Mm}^{-1}$  in the warm period; both values approximately 5 times  
321 less than those observed at IBS.

322 Monthly means of  $b_{abs}(880)$  for each year together with intra-annual means for IBS are  
323 shown in [Figure 2](#). Specifically, annual average  $b_{abs}(880)$  exhibits a significant peak during  
324 winter and summer for any year. The examination of the overall changes by the inter-annual mean  
325 reveals a gradual increase from November ( $0.4 \pm 0.5 \text{ Mm}^{-1}$ ) to February ( $0.9 \pm 0.8 \text{ Mm}^{-1}$ ); the latter  
326 represents the maximum light absorption observed at IBS. In February, the monthly mean of  
327  $b_{abs}(880)$  ranged from 0.4 to  $1.7 \text{ Mm}^{-1}$  reaching the maximum ( $1.7 \text{ Mm}^{-1}$ ) in 2022. Thus, Arctic  
328 haze is present at IBS in winter months, from December to February. Starting from March ( $0.6 \pm 0.5$   
329  $\text{Mm}^{-1}$ ), the inter-annual mean decreased down to a minimum in June ( $0.1 \pm 0.2 \text{ Mm}^{-1}$ ) that was 9  
330 times less than that of February. August had the highest light-absorption (mean:  $0.7 \pm 2.2 \text{ Mm}^{-1}$ )  
331 within the summer months, ranging from 0.2 to  $1.5 \text{ Mm}^{-1}$  and showing a maximum of 1.5 in 2021.  
332 September and October demonstrated a similar level of variability with June. At Zeppelin, the  
333 maximum of the intra-annual (2001-2015) mean was seen in March - April ( $0.3 \text{ Mm}^{-1}$ )  
334 (Stathopoulos et al., 2021), coinciding with the Arctic haze phenomenon in late winter-spring that  
335 has been widely observed in the European and Canadian Arctic (Sharma et al., 2004; Schmale et al.,  
336 2022).

337 In order to relate the light absorption in visible spectrum to the variability on other locations  
338 (Schmeisser et al., 2018; Pulimeno et al., 2024), we calculate  $b_{abs}$  at 520 and 590 nm. The mean  
339 (median) value of  $b_{abs}(520)$  was  $0.9 \pm 1.6$  ( $0.5$ )  $\text{Mm}^{-1}$  for the entire study period ([Table 1](#)). At Ny-  
340 Ålesund (Svalbard), the annual mean (median)  $b_{abs}(530)$  averaged for 2018 to 2022 was 0.22  
341 ( $0.13$ )  $\text{Mm}^{-1}$  (Pulimeno et al., 2024), approximately 4 times less. Moreover, the absorption  
342 coefficient  $b_{abs}(550)$  of 0.18 ( $0.09$ )  $\text{Mm}^{-1}$  recorded for 2012-2014 again in Svalbard (Schmeisser  
343 et al., 2018) was 4 times less compared to annual average light absorption at IBS.

344 We present multi-annual box-and-whisker plots of  $b_{abs}$  at 590 nm in [Figure 3](#). The  
345 wavelength of 590 nm was chosen as the closest to 550 nm reported for the polar station Tiksi  
346 (Schmeisser et al., 2018; Schmale et al., 2022). The monthly medians of  $b_{abs}(590)$  in February  
347 ranged from 0.3 to  $2.3 \text{ Mm}^{-1}$ , representing the highest values observed in 2022. The highest  
348 extended interquartile range (up to  $1 \text{ Mm}^{-1}$ ) was observed in the cold period. Conversely, the  
349 summer months exhibited a minimum of approximately  $0.1 \text{ Mm}^{-1}$  for  $b_{abs}(590)$  with smaller  
350 variation of data characterized by the low interquartile range of  $0.4 \text{ Mm}^{-1}$ .

351 The annual cycle of  $b_{abs}(590)$  reflects the higher aerosol burden during the haze season and  
352 the low concentrations during summer at Alert, Barrow/Utqiagvik, Zeppelin, Gruvebadet, and Tiksi

Deleted: Figure 2

Deleted: Table 1

Deleted: Figure 3

(Schmale et al., 2022). Seasonality of  $b_{abs}$  medians at 550 nm for polar stations (Alert, Barrow/Utqiagvik, Tiksi, Zeppelin) from (Schmeisser et al., 2018) and  $b_{abs}(590)$  for IBS are presented in **Figure 3**. All sites demonstrate similar seasonal variations, albeit a different magnitude of light absorption. In February, the maximum  $b_{abs}(590)$  ( $1.1 \text{ Mm}^{-1}$ ) was observed at IBS; a higher value has been only observed at Tiksi which is explained by the influence from local sources (Popovicheva et al., 2019a). Other stations show the Arctic haze maximum later (in March or April); a sharp decline of  $b_{abs}(590)$  was observed at those months at IBS. Values similar to other Arctic stations were recorded at IBS in June, with an annual minimum of around  $0.1 \text{ Mm}^{-1}$ . Since July,  $b_{abs}(590)$  at IBS was higher than at other stations except Tiksi and peaked at  $0.8 \text{ Mm}^{-1}$  in December. The polar station Pallas exhibits the opposite behaviour peaking in spring and summer (Schmeisser et al., 2018). Pallas is located relatively south as compared to the rest of the polar stations and, hence, it is influenced by anthropogenic and biogenic emissions from surrounding boreal forests (Asmi et al., 2011). Aerosol optical properties in the IR and visible solar spectrum at IBS are different from European, Canadian and Western high-latitude polar locations due to different source origins, but light absorption coefficients are higher during the haze period (December-February).

Deleted: Figure 3

### 3.2 Black carbon and site-specific mass absorption cross-section

EC collocated with light absorption observations is widely used to infer BC (Grange et al., 2020). **Figure 4a** shows concentrations of EC determined for samples collected in parallel with the aethalometer measurements from 10 August 2019 to 31 December 2022, with  $eBC_{AET}$  concentrations averaged over the sampling period. Both weekly EC and  $eBC_{AET}$  concentrations show the same seasonal variations with a maximum in winter and minimum in summer. EC concentrations are generally smaller than  $eBC_{AET}$ . The annual EC mean concentrations ranged from  $6.5$  to  $16.3 \text{ ng C m}^{-3}$ . The highest EC ( $0.2 \text{ } \mu\text{g C m}^{-3}$ ) was recorded in December 2019 and the highest  $eBC_{AET}$  ( $0.4 \text{ } \mu\text{g C m}^{-3}$ ) in December 2019 and January 2022. EC was higher ( $0.05 \pm 0.03 \text{ } \mu\text{g C m}^{-3}$ ) in the cold period and decreased ( $0.02 \pm 0.03 \text{ } \mu\text{g C m}^{-3}$ ) in the warm period (**Table 1**). Annual average mean EC during the entire study period was  $0.03 \pm 0.03 \text{ } \mu\text{g C m}^{-3}$ . For comparison, at Zeppelin and Villum the annual mean EC concentrations were  $0.012 \pm 0.04 \text{ } \mu\text{g C m}^{-3}$  (2017-2020) (Yttri et al., 2024) and  $0.029 \pm 0.03 \text{ } \mu\text{g C m}^{-3}$  (2011-2013) (Massling et al., 2015), respectively.

Deleted: Figure 4

Annual mean OC concentrations during the entire study period were estimated as  $0.45 \pm 0.3 \text{ } \mu\text{g C m}^{-3}$ . At Zeppelin, annual OC (2017-2020) was 3.5 smaller ( $0.13 \pm 0.1 \text{ } \mu\text{g C m}^{-3}$ ) (Yttri et al., 2024). Notably, the multi-year average EC and OC levels at IBS are approximately 3 times higher than at Zeppelin, that correlates well with increased light absorption, as described previously. At IBS, OC was  $0.4 \pm 0.2 \text{ } \mu\text{g C m}^{-3}$  in the cold period and increased to  $0.5 \pm 0.4 \text{ } \mu\text{g C m}^{-3}$  in warm period, opposite

Deleted: Table 1



to EC (Table 1). The ratio OC/EC shows increased OC and decreased EC in the warm period and an opposite trend in the cold (Figure 4b). Figure 4c depicts the relationship between  $eBC_{AET}$  and EC in cold and warm periods. We note the high  $R^2$  values for the cold period (0.88) and slightly lower ones for the warm one (0.78). During the warm period, seasonal mean values reveal an overestimation of  $eBC_{AET}$  that is more pronounced during the warm period, with a slope equal to 2.3.  $R^2$  values were lower because many EC values were close to the LOD. Seasonal differences are attributed to pollutant sources altering the chemical composition of aerosol at IBS. A positive correlation was observed between  $eBC_{AET}/EC$  and OC/EC indicating that BC at IBS is coated with OC leading to the lens effect (Kanaya et al., 2008) and overestimating  $eBC$ .

Similar seasonal variation for  $eBC$  and EC with highest winter and lower summer concentrations has been observed previously at Villum, with a regression slope of 2 and a  $R^2$  of 0.64 (Massling et al., 2015). At Alert, the median  $SAC$  during the Arctic haze season (November to April) was  $19.8 \text{ m}^2 \text{ g}^{-1}$  (Sharma et al., 2004). However, during the non-Arctic haze period from May to October it was significantly higher  $28.8 \text{ m}^2 \text{ g}^{-1}$  and much more variable. This is explained by aged, internally mixed, and of anthropogenic origin of winter and spring arctic aerosols while summer aerosols were affected by local sources.

Following the definition in Eq.5, we calculate the  $SAC$  from the slope of BC light absorption at 880 nm,  $b_{abs/BC}(880)$ , and EC concentrations.  $SAC_{BC,cold}$  (for the cold period) was estimated to be  $15.9 \text{ m}^2 \text{ g}^{-1}$  while  $SAC_{BC,warm}$  was higher ( $18.1 \text{ m}^2 \text{ g}^{-1}$ ) (Figure 5).  $SAC$  values at Alert have been reported to be even higher (Sharma et al., 2004), showing that Western Arctic aerosols differ by composition and aging. Recalculations of BC mass with  $SAC$  values for cold and warm periods ( $eBC$ ), separately, were performed according to Eq.1.

Timeseries of daily and monthly mean  $eBC$  concentrations from August 2019 to 31 December 2022 are shown in Figure 2. Annual mean and median  $eBC$  for the entire period were  $28.7 \pm 54.1 \text{ ng m}^{-3}$  and  $12.5 \text{ ng m}^{-3}$ , respectively (Table 1); they exhibit a strong year-by-year variability. We note that the  $eBC$  values are approximately half of the  $eBC_{AET}$  value. Previous studies have evaluated the optical properties of BC against direct mass measurements techniques and also obtained MAC values depending on the location, different from the recommended by aethalometer (Sharma et al., 2004; Eleftheriadis et al., 2009; Yttri et al., 2024). For example, the relationship between  $BC_{AET}$  and EC obtained by the thermal technique at Alert station (Canada) during 3 - year measurements was 0.85 (Sharma et al., 2004). Studies at Villum Research Station (Greenland) showed good agreement between measured EC and  $eBC_{AET}$  concentrations (Massling et al., 2015) similar to our study.  $eBC$  climatology and the statistics for each month and year of study are

Deleted: Table 1

Deleted: Figure 4

Deleted: Figure 4

Deleted: Figure 5

Deleted: Figure 2

Formatted: Font: Not Italic, Check spelling and grammar

Deleted: Table 1

Formatted: Font: Not Italic, Check spelling and grammar

presented in **Figure 2** and **Table S 2**, respectively. The annual mean *eBC* in 2019, 2021 and 2022 was  $33\pm44$ ,  $33\pm85$ , and  $32\pm48$  ng m<sup>-3</sup>, respectively, for the entire study period. Statistically significant difference at the 95% confidence level (p-value <0.05, t-test) was observed for the cold and warm periods with means of  $44\pm47$  and  $19\pm57$  ng m<sup>-3</sup>, respectively. The smallest mean *eBC* of  $24\pm29$  ng m<sup>-3</sup> occurred in 2020. The latter is likely attributed to the impact of COVID-19 restriction measures to the emissions of BC (Evangelidou et al., 2020).

The general trend of the maximum in winter and minimum in summer well reproduces the typical *eBC* seasonality reported in polar observatories (Stone et al., 2014; Schmale et al., 2022). **Figure 2** shows monthly mean *eBC* concentrations for half of year 2019 and whole - year periods of 2020, 2021, and 2022 as well as annual averaged monthly mean *eBC* climatology for the entire study period. The highest concentration in the cold period was observed in December 2019 ( $81\pm64$  ng m<sup>-3</sup>), January 2022 ( $61\pm49$  ng m<sup>-3</sup>), February 2022 ( $106\pm67$  ng m<sup>-3</sup>), and March 2021 ( $42\pm33$  ng m<sup>-3</sup>) (**Table S 2**). In warm periods we recorded the highest concentrations in September 2020 ( $31\pm48$  ng m<sup>-3</sup>), August 2021 ( $83\pm249$  ng m<sup>-3</sup>), April 2021 ( $35\pm 26$  ng m<sup>-3</sup>), and August 2022 ( $28\pm54$  ng m<sup>-3</sup>).

### 3.3 Multi-wavelength absorption Angstrom exponent

As shown by Virkkula (2021), pure BC particles surrounded by non-absorbing coatings can have *AAE* in the range from <1 to 1.7. Compendium of values from different emissions show *AAE* variation from 0.2 to 3.0 for transport, power plants, and domestic wood burning (Helin et al., 2021). Primary emissions from residential heating (Cuesta-Mosquera et al., 2024) and BB (Popovicheva et al., 2017a, 2019b) have been associated with high *AAE* of around 3-4. Due to the mixing with background aerosol, coating and aging processes, a large change in the light absorption has been reported at receptors of long-range transported pollution (Cappa et al., 2016). For highly aged aerosols, *AAE* has been found lower than 1.0 due to large and internally mixed particles (Popovicheva et al., 2022). Spectral absorption was obtained at IBS in the UV to IR spectral region emphasized by the value of *AAE*<sub>350/950</sub> equal to 0.96 for the entire study period (**Figure 6a**). Power law fittings of spectral dependence for both and cold periods show similar values, indicating highly mixed and aged BC.

Multiple studies have addressed the sensitivity of the *AAE* to the range of wavelengths selected for its calculation (Cuesta-Mosquera et al., 2024); the extent of this sensitivity is higher for aerosols containing a substantial contribution of organic species such as BrC. Events affected by regional fire emissions were evident by the light absorption coefficient *AAE*<sub>370/520</sub> in the short wavelength range (Ulevicius et al., 2010). In remote Arctic environments, cases with exceeded *AAE*<sub>467/660</sub> have been identified to be influenced by BB (Pulimeno et al., 2024). Impact of

Deleted: Figure 2

Deleted: Table S 2

Deleted: Figure 2

Deleted: Table S 2

Deleted: Figure 6

intensive wildfires in North America on aerosol optical properties measured at the European Arctic has been associated with increased daily  $AAE_{467/660}$  of up to 1.4 (Markowicz et al., 2016). Strong UV absorption has led to increase of up to 1.8, clearly indicating the importance of non-BC light-absorbing component (Ran et al., 2016).

To apportion the wavelength-dependent light absorption, we used a pair of wavelengths (350 and 950 nm) in the whole spectrum, and in shorter wavelengths (370 and 660 nm, 370 and 520 nm). Timeseries of weekly average  $AAE_{370/520}$  showed a similar seasonality but wider variation (0.2-3.1) than (0.5-1.7) for  $AAE_{370/950}$  (Figure 6b). The mean values increased from  $0.97 \pm 0.23$  for  $AAE_{370/950}$  to  $1.17 \pm 0.5$  for  $AAE_{370/520}$  for the entire study period (Table 1). Box-whisker plots and annual averaged means of  $AAE_{370/950}$  showed no prominent monthly dependence (Figure 4c). However, increased  $AAE_{370/950}$  above 1.1 was observed in summer months for several years, in July 2020, June 2021 and from May to September 2022 (Table S 2). The shorter the wavelength pair, the higher the annual average  $AAE$  above 1.0. The largest values of monthly mean (median)  $AAE_{370/520}$  were found for April to September with a maximum in June. Such considerable deviation during warm months implies the importance of BrC light-absorbing components within highly mixed Arctic aerosols at IBS.

Light absorption at 370 nm,  $b_{abs}(370)$ , was used to estimate the BrC mass concentrations. The mean (median) value of  $b_{abs}(370)$  was 2.4 times higher than  $b_{abs}(880)$  for the entire study period as well as for cold and warm ones (Table 1). Monthly means and box-whisker plot of  $b_{abs}(370)$  showed trends similar to  $b_{abs}(880)$  (Figure S 4). Assuming that the wavelength pair  $\lambda$  and  $\lambda_0$  in Eq. 3 being 370 and 950 nm, respectively, the absorption coefficient for BrC at 370 nm,  $b_{abs/BrC}(370)$ , is determined by subtracting BC absorption from the total absorption at the same wavelength using the  $AAE_{370/950}$  value for entire period (Table 1). Monthly  $b_{abs/BrC}(370)$  and  $b_{abs/BrC}(370)$  as well as the  $b_{abs/BrC}(370)$  percentage contribution to total  $b_{abs}(370)$  are shown in Table S 3 for those years when the contribution of BrC absorption was higher than 1%. We note 13% for August 2021 for the warm period and 5 % for February 2022 and December 2021 for the cold period.

### 3.4 Modelled concentrations of BC

Figure 7a shows the monthly mean  $eBC$  and surface BC ( $BC_{FLEXPART}$ ) concentrations simulated with FLEXPART coupled to ECLIPSEv6-GFAS emissions for the entire study period. FLEXPART model performs well in capturing the seasonality of observed features with both high and low concentrations. Annual mean modelled  $BC_{FLEXPART}$  ( $88.4 \text{ ng m}^{-3}$ ) is 37% higher than  $eBC_{AET}$  ( $64.3 \text{ ng m}^{-3}$ ) and 3 times higher than  $eBC$  ( $29.5 \text{ ng m}^{-3}$ ). Annual and monthly means of

Deleted: Figure 6

Deleted: Table 1

Deleted: Figure 4

Deleted: Table S 2

Deleted: Table 1

Deleted: Figure S 4

Deleted: Table 1

Deleted: Table S 3

Deleted: Figure 7

513  $eBC_{AET}$  show values closer to  $BC_{FLEXPART}$  than  $eBC$ . This is a reasonable finding because the  
 514 global emission datasets could not consider local pollution. Almost all simulated BC  
 515 concentrations, except in February 2020 and 2021, were found within the standard deviation range  
 516 of measured  $eBC_{AET}$ . A good correlation between measurements and simulations, with a Pearson  
 517 coefficient of 0.72 and 0.82, a root mean squared error (RMSE) of  $15 \text{ ng m}^{-3}$  and  $0.14 \text{ ng m}^{-3}$  and a  
 518 normalised bias of 0.39 and 0.27 was obtained for the cold and warm period, respectively (Figure  
 519 7b,c).

520 FLEXPART does not reproduce seasonal variations of BC everywhere over the Arctic.  $R^2$   
 521 and RMSE varied between 0.53-0.80 and  $15.1\text{-}56.8 \text{ ng m}^{-3}$ , respectively, depending on the location  
 522 (Zhu et al., 2020). At Zeppelin, modelled BC (annual mean of  $39.1 \text{ ng m}^{-3}$ ) was reported to be 85%  
 523 higher than the measured value ( $21.1 \text{ ng m}^{-3}$  for annual mean). At Tiksi, modelled BC was  
 524 underestimated ( $74.4 \text{ ng m}^{-3}$  for annual mean) by 40% compared with observations ( $104.2 \text{ ng m}^{-3}$  for  
 525 annual mean) (Zhu et al., 2020). Such good result for IBS is due to its closer location to the biggest  
 526 emission sources.

527 Figure 8 shows the vertical distribution of simulated BC as a function of time for 2019-2020  
 528 years (vertical cross-section). Consistently high vertical BC profiles up to 2 km were observed in  
 529 the cold period, except in April 2022. In February 2020, a smoke layer of BC concentrations of up  
 530 to  $100 \text{ ng m}^{-3}$  was prominent at up to 4 km. On the contrary, in the warm period the smoke resides  
 531 near the surface, despite a few events of extremely high vertical BC at altitudes up to 8 km and 10  
 532 km, which occurred in July 2020 and August 2021, respectively. Nevertheless, the evidence of  
 533 atmospheric transport from high altitudes during summer months is evident by the elevated  
 534 modelled BC ( $>100 \text{ ng m}^{-3}$ ) at high model layers (e.g., July 2019, June-August 2020, June-July  
 535 2021 and May-June 2022). In all these periods,  $BC_{FLEXPART}$  (gray line in Figure 8) was under  $40 \text{ ng}$   
 536  $\text{m}^{-3}$  showing that the emission sources are probably far away, and that long-range transport  
 537 occurred. The low injection altitude of anthropogenic emissions in winter months cause emitted  
 538 substances to remain close to the emission sources. BC climatology at IBS indicates that the long-  
 539 range transported anthropogenic emissions in the cold period reside at altitudes up to 2 km and  
 540 compose a persistent layer (Figure 8). This is further explained by the rapid (about 4 days, or less)  
 541 low-level transport of air masses to the Arctic troposphere as described in Stohl (2006). However,  
 542 this cannot be confirmed without targeted high altitude observations.

Deleted: Figure 7

Deleted: Figure 8

Deleted: violet

Deleted: Figure 8

Deleted: Figure 8

548 **4 Discussion**

549 **4.1 Long-range transport, age and region contributions**

550 Transport mechanisms from the source regions affect the Arctic BC variability and burden  
551 (Chen et al., 2023; Zhou et al., 2012). Transport of aerosols to the Arctic leads to high  
552 concentrations of BC in winter and spring (Arctic haze) and low values in summer (Law and Stohl,  
553 2007) when the removal processes in the dry and stable Arctic atmosphere are very slow. Synoptic-  
554 scale circulation effects promote the effective transport from lower latitudes, namely diabatic  
555 cooling of air masses moving over snow-covered ground, high continental pressure in winter, and  
556 the intrusion of warm air from lower latitudes (Gilardoni et al., 2023). Seasonal trends of footprint  
557 emission sensitivity demonstrate the transport mechanisms from the source regions to the European  
558 Arctic (Platt et al., 2021). BC at Zeppelin is affected by significantly different source regions during  
559 the warm and cold seasons, while large-scale circulation patterns that affect the pollutant transport  
560 from lower latitudes show the opposite behaviour during these two periods (Stathopoulos et al.,  
561 2021).

562 **Figure 9**, shows a 3.5-year climatology of the surface footprint emission sensitivities at IBS.  
563 From December to February, anthropogenic polluted air mass transportation takes place from  
564 Eurasia (territories above 40°N), as illustrated by the elevated footprints there. The extension of the  
565 Arctic front towards lower latitudes during the cold period facilitates such transport (Stohl, 2006).  
566 The warmer it gets in spring, the narrower the area of emission transport. In the transition from  
567 spring to summer, transport patterns and meteorological conditions change, such as that the  
568 advection of the particulate pollution to the Arctic boundary layer from lower latitudes becomes  
569 limited (Bozem et al., 2019). In JJA (June, July, August) footprint is mostly restricted to coastal  
570 regions of Eurasia, Greenland, and North America and does not extend deeply into the continents.  
571 This is a consequence of the so-called ‘polar dome’ that prevents warm continental air masses from  
572 entering the Arctic lower troposphere (Stohl, 2006). As a result, anthropogenic pollution becomes  
573 less significant, and natural aerosol sources prevail (Moschos et al., 2022b, a). In autumn  
574 (September, October, November), footprint is similar to the MAM (March, April, May) one  
575 completing the annual cycle.

576 For the entire study period, the monthly mean contribution to surface BC for all years was  
577 from air masses with 1-3 (31%) and 3-6 days (22%) aging (**Table S 4**). The highest BC contribution  
578 (34%) and (39%) was observed for the shortest age of 1-3 days in DJF (December, January,  
579 February) and MAM, respectively (**Figure 8**). In summer, the highest BC contribution (35%) was  
580 replaced by a longer age of 6-9 days.

Deleted: Figure 9

Deleted: Table S 4

Deleted: Figure 8

Footprint emission sensitivities of Arctic air masses also constrain the region contributions. The major source regions contributing BC to IBS are the territory of the Russian Federation (including European part of Russia (EURus), Siberia, Far East), Asia, Europe, Northern America, and Ocean. Due to the geographical proximity, EURus/Siberia/Far East contribution (77%) dominated during the entire study period on a basis of the annual average monthly means (Table S 4), with a maximum of 83% in SON (Figure 9). Its monthly maximum (88%) was recorded in September 2021, and the minimum (60%) in June 2022. Europe was the second region contributor (11%) followed by Asia. The monthly mean contribution of Northern America was up to 12% in JJA, the largest was observed in July 2022 (62%).

#### 4.2 Anthropogenic and biomass burning sources

The time series of monthly mean and annual average monthly mean source contributions to surface BC at IBS are shown in Figure 10a. Anthropogenic sources (DOM, TRA, IND, FLR, All others) contribute 97% of the total for the entire study period (Table S 4). A decrease from winter to July and an increase from August to winter were seen. In the cold period, air masses arrived at IBS through the populated regions of Western Europe, EURus, Siberia, and Asia, crossing the biggest oil and gas extraction regions of Kazakhstan, Volga-Ural, Komi, Nenets, and Western Siberia (Figure 1). Because IBS is located north of the largest oil and gas producing regions of Western Siberia, high FLR contribution of 59% and 32% was observed both in the cold and warm period (Table S 4). Annual mean contributions to modelled surface BC from FLR, DOM, TRA, and IND sectors dominated in January and December (60%, 22%, 12%, and 9%, respectively). All other sources were around 2% at that time. BB played the biggest role between April (8%) and October (17%), with maximum in August (80%).

Figure S 5 shows the percentage sectoral contributions on monthly mean BC concentrations for 2021 and 2022, data for 2019 and 2020 was shown in Figure 10a. February 2021 and December 2021 were the leaders of FLR impact with 67.2% and 67.4%, respectively. During February 2022 of the record high BC pollution level observed at IBS, air masses arrived at IBS through the Western Europe, EURus, and Siberia, passing through the flaring facilities of Kazakhstan, Volga-Ural, Komi, Nenets, and Western Siberia. They caused of 50%, 26%, 15%, 8%, 0.2%, and 3.3% monthly average contribution to surface BC from FLR, DOM, TRA, IND, BB and All other sources, respectively. Footprint emission sensitivities on 3rd February 2022 at 12:00-15:00 when eBC reached 310 ng m<sup>-3</sup> (Figure S 5) showed air mass transport to IBS straight through the Western Siberian gas flaring region (Figure 10b).

The contribution of FLR dropped significantly from April to a minimum of 18% in June and rose in September. In the winter months when the overestimation of modelled BC concentrations

Deleted: Table S 4

Deleted: Figure 9

Deleted: Figure 10

Deleted: Table S 4

Formatted: Font: Not Bold

Formatted: Font: Not Bold, Not Italic, Check spelling and grammar

Deleted: Figure 1

Formatted: Font: Not Bold

Formatted: Font: Not Bold, Not Italic, Check spelling and grammar

Deleted: Table S 4

Formatted: Font: Not Bold

Formatted: Font: Not Bold, Not Italic, Check spelling and grammar

624 was recorded (see section 3.4), the highest FLR impact was seen. DOM showed the biggest  
625 contribution (18%) from November to February, exactly during the heating season. The light  
626 absorption of BrC was significant mostly in wintertime (Table S 3). The latter indicates significant  
627 impact of biomass used for domestic heating, in accordance to wood burning contribution of 61% of  
628 the total residential emissions in forest regions (Huang et al., 2015).

629 According to CAMS GFAS (Figure S 3), significant global fire emissions started from June  
630 and lasted until the mid of November in 2020 and 2022; the period of fire emissions was shorter but  
631 more intensive from July until September 2021. At IBS, the annual mean BB contribution  
632 approached 48% of the total in the warm season (Table S 4). It started increasing from April and  
633 approached a maximum of 80% in August, whereas TRA, DOM, IND, and All other sources were  
634 minimum. From middle June to September, the average monthly BB contribution was larger than  
635 all anthropogenic sources. Notably, from April to September, the high mean BB contribution was  
636 related to the excess of  $AAE_{370/520}$  over 1.0 (maximum: 1.7 in July) (Figure 6). At that time, the air  
637 masses transported to IBS were aged ( $> 6$  days) dominating the age spectrum (57%) (Table S 4).

638 In 2019, 72,400 km<sup>2</sup> were burned in Siberia or 42% of the total burned area that occurred in  
639 Russia (Voronova et al., 2020). A significant relationship between the burned areas and associated  
640 pyrogenic emissions with atmospheric blocking events was reported (Mokhov et al., 2020). August  
641 and September showed 50% and 35%, respectively, monthly mean BB contributions, while October  
642 and November lower, 30% and 20%, respectively (Figure S4).

643 In spring 2020, BB BC concentrations simulated with WRF-Chem model were distributed in  
644 areas between 40°N and 60°N in Europe, central Siberia, and East Asia, and indicated intensive  
645 seasonal agriculture fires in Europe and Siberia (Chen et al., 2023). Spring fires contributed about  
646 12% BB BC to IBS (April and May). The end of June and beginning of July of 2020 was  
647 characterized by high altitude BC (Figure 8) indicating high altitude long-range transport. A high  
648 BrC content was also observed in July and September 2020 (Table S 3).

649 In 2021, the monthly mean spring BB contribution approached a maximum of 36% in May.  
650 Yakutia (Eastern Siberia) experienced the worst fire season over the last four decades (Tomshin and  
651 Solovyev, 2022). Around 150,000 fires occurred, almost twice as much as the previous year  
652 (Voronova et al., 2022). August 2021 received 90% contribution from BB as compared to all the  
653 other sources. At that time unprecedented high smoke levels were recorded over Western Siberia  
654 (Schneider et al., 2024). Satellite image reveals the strong plume from the area of Yakutian  
655 wildfires which brought deep smoke to IBS located around 2000 km far away (Figure 1c). The  
656 highest  $eBC$  level of 1800 ng m<sup>-3</sup> on 5th August, exceeded the 75th percentile of the entire period

Deleted: Table S 3

Formatted: Font: Not Bold

Formatted: Font: Not Bold, Not Italic, Check spelling and grammar

Deleted: Figure S 3

Formatted: Font: Not Bold, Font colour: Auto

Formatted: Font: Not Bold, Not Italic, Font colour: Auto, Check spelling and grammar

Deleted: Table S 4

Formatted: Font: Not Bold

Formatted: Font: Not Bold, Not Italic, Check spelling and grammar

Deleted: Figure 6

Formatted: Font: Not Bold

Formatted: Font: Not Bold, Not Italic, Check spelling and grammar

Deleted: Table S 4

Formatted: Font: Not Bold

Formatted: Font: Not Bold, Not Italic, Check spelling and grammar

Deleted: Figure 8

Formatted: Font: Not Bold

Deleted: Table S 3

Formatted: Font: Not Bold

Formatted: Font: Not Bold, Not Italic, Check spelling and grammar

Deleted: Figure 1

Formatted: Font: Not Bold

Formatted: Font: Not Bold, Not Italic, Check spelling and grammar



53 times (Table 1). The measured concentrations were 180 times higher than the Arctic background (Figure S 6). Severe smoke affected the visibility near IBS (Figure 1d). Footprint emission sensitivity on 5th August (from 18:00 to 21:00) at the time when *eBC* peaked (1540 ng m<sup>-3</sup>) confirms that air masses originated from Yakutia and arrived to IBS from the northeast direction (Figure 10b). BC for these wildfires was transported at altitude as high as 10 km (Figure 8). Finally, in summer 2022, wildfires took place in Western Siberia and the EURus (Popovicheva et al., 2023); BB contributions in June, July, August 2022 were around 65%, whereas light absorption of BrC was important in May and August 2022 (Table S 3).

## 5 Summary and conclusions

We presented four years (2019-2022) of observations at the aerosol station IBS with respect to light-absorption characteristics of Western Siberian polar aerosols and its basic cycles, such as seasonality, annual means, and interannual variability. The annual cycle of multi-wavelength light absorption demonstrates higher levels during the Arctic haze season and lower in summer, similar to other Arctic observations. The light absorption coefficient revealed several unique features:

Higher values of the light absorption coefficient (around 4-5 times) in comparison with multi-year observations at high-latitude polar stations in European Arctic (annual mean of  $0.7 \pm 0.7$  M m<sup>-1</sup> in the cold season and 2 times lower in warm). Wintertime maximum was observed in February ( $0.9 \pm 0.8$  M m<sup>-1</sup>) that coincides with the Arctic haze peak; this is different from the European and Canadian Arctic that is usually observed in early spring. The interannual minimum was observed in June whereas August was highly variable with respect to light-absorption due to the Siberian wildfires. Multi-annual monthly means for  $b_{abs}(880)$  in the visible spectrum at IBS were found higher than at European, Canadian and Western high-latitude polar locations, due to that IBS is closer to the main Northern Eurasian source regions.

Wildfires caused increased concentrations, usually in August. Increase of the AAE in the UV spectrum between April and September implies coexistence of highly mixed/aged BC and light-absorbing BrC components. Specifically, monthly BrC contribution to total light absorption was 5% in February 2022 and 13% August 2021 likely due to wildfire impact. BrC light absorption coefficient in the UV spectrum showed similar trends as BC, although it exceeded BC by 2.4 times during both cold and warm periods. AAE was equal to 0.96, indicating highly mixed and aged aerosols. AAE in UV spectrum increase up to  $1.17 \pm 0.5$  implies coexistence of light-absorbing BrC components in BB aerosols, with the biggest impact between April and September.

We calculated SAC for the first time at IBS by combining multi-year optical absorption and EC data. Higher SAC of 18.1 m<sup>2</sup> g<sup>-1</sup> in the warm period than in the cold one (15.9 m<sup>2</sup> g<sup>-1</sup>) revealed

Deleted: Table 1

Formatted: Font: Not Bold, Font colour: Auto, English (UK)

Formatted: Font: Not Bold, Not Italic, Font colour: Auto, English (UK), Check spelling and grammar

Deleted: Figure S 6

Deleted: Figure 1

Formatted: Font: Not Bold

Formatted: Font: Not Bold

Formatted: Font: Not Bold, Not Italic, Check spelling and grammar

Deleted: Figure 10

Deleted: Figure 8

Formatted: Font: Not Bold

Deleted: Table S 3

Formatted: Font: Not Bold

Formatted: Font: Not Bold, Not Italic, Check spelling and grammar

Deleted: Higher magnitude



influence from non-BC light-absorbing species, such as organic matter and mineral dust; SAC values were lower than those observed in the Canadian Arctic indicating different aerosol composition and aging. Mean eBC in the cold and warm periods were equal to  $44 \pm 47$  and  $19 \pm 57$  ng m<sup>-3</sup>, respectively. Record high eBC was found in February 2022 ( $106 \pm 67$  ng m<sup>-3</sup>) and August 2021 ( $83 \pm 249$  ng m<sup>-3</sup>) during the years of study.

Observations at the IBS station evaluated the relationship between  $eBC_{AET}$  and EC under specific atmospheric conditions.  $eBC$ , recalculated using site-specific absorption coefficients, reflects seasonal variations and provides insights into aerosol composition. Annual cycles follow typical Arctic trends, with higher  $eBC$  concentrations in winter when air masses primarily originate from Russia, Siberia, the Far East, Europe, and Asia. During this period, black carbon from gas flaring dominates, particularly in January, when air masses pass over oil and gas facilities in Kazakhstan, Volga-Ural, Komi, Nenets, and Western Siberia. In summer, biomass burning (BB) from Siberian wildfires surpasses anthropogenic sources, peaking in August 2021, which saw the worst fire season in four decades, bringing heavy smoke to IBS. February 2022 also recorded extreme BC pollution levels.

Modeling analyses indicate that 77% of BC transport originated from Russia, Siberia, and the Far East, followed by Europe (11%), Asia (7%), and North America (4%). In winter, air masses traveled 1-3 days from Eurasia (north of 40°N) to IBS, whereas in summer, transport took 6-9 days. Low-injection altitude anthropogenic emissions created a persistent BC layer up to 2 km in the cold season, reaching 4 km in February 2020, with record concentrations of 100 ng m<sup>-3</sup>. In contrast, wildfire smoke in summer elevated BC layers to higher altitudes.

Anthropogenic emissions accounted for 83% of BC during the study period, dominated by gas flaring (FLR, 59%), domestic heating (DOM, 18%), traffic (TRA, 10%), and industry (IND, 7%) during Arctic haze period. Gas flaring remained the primary contributor year-round (59% in winter, 32% in summer), given IBS's proximity to major oil and gas regions. Residential heating peaked in winter (18%), aligning with enhanced brown carbon (BrC) absorption from wood burning. In February 2022, modeled BC concentrations reached 310 ng m<sup>-3</sup> as air masses passed through major flaring regions, though overestimation suggests miscalculated source intensities.

BB contributions peaked at 48% in the warm season, surpassing anthropogenic sources from mid-June to September, with a maximum of 80% in August. Extreme vertical BC events reached 8 km in July 2020 and 10 km in August 2021 due to wildfires. In May 2021, BB contributions reached 36% due to strong agricultural fires in Siberia, while in August 2021, 90% of BC at IBS originated from Yakutia's wildfires, 2000 km away.

The increasing intensity and frequency of wildfires at high latitudes highlight the importance of carbonaceous aerosol measurements. These observations provide critical insights into Arctic

740 aerosol radiative properties, particularly in the UV-VIS spectrum, where enhanced light absorption  
741 contributes to amplified Arctic warming, especially in summer.

742

743

744 **Data availability.** All modelling data from this study are available for download from [https://atmo-](https://atmo-access.nilu.no/BELY2_MSU.py)  
745 [access.nilu.no/BELY2\\_MSU.py](https://atmo-access.nilu.no/BELY2_MSU.py). FLEXPART version 10.4 model can be downloaded from  
746 <https://www.flexpart.eu/downloads>. Black Carbon observations are available upon request from O.  
747 B. Popovicheva.

748

749 **Supplement.** The supplement related to this article is available online at.

750

751 **Author contributions.** OBP supervised the station operation, interpreted data and wrote the  
752 manuscript. NE performed all the FLEXPART simulations and analyses, wrote and coordinated the  
753 paper. MAC analysed the data, prepared the figures and assisted in the interpretation of the results.  
754 ED provided supported AAE calculations and evaluation of data quality. NSK supported the  
755 research. All authors contributed to the final version of the manuscript.

756

757 **Competing interests.** The authors declare no competing interests.

758

759 **Acknowledgements.** This research was performed in the frame of the development program of the  
760 Interdisciplinary Scientific and Educational School of M. V. Lomonosov Moscow State University  
761 (MSU) “Future Planet and Global Environmental Change”. For instrument calibration, the  
762 equipment of MSU Shared Research Equipment Center “Technologies for obtaining new  
763 nanstructured materials and their complex study” was used. This equipment was purchased by  
764 MSU in the frame of the Equipment Renovation Program (National Project “Science”). Authors  
765 thank Magee Scientific for AE33 instrumentation support and Dr. Asta Gregorič for data  
766 examination. V.O. Kobelev is acknowledged data analyses over all study years.

767

768 **Financial support.** The article processing charges for this publication were paid by NILU.  
769 Developed methodology of aethalometric measurements was implemented in the frame of the RSF  
770 project #19-77-3004II. Authors thanks to Russian Geographical Society for the data treatment  
771 support Institute of Environmental Survey, Planning and Assessment (IESPA) partly supported the  
772 instrumentation and power supply of IBS.

773

774 **References**

**Deleted:** This research was performed in the frame of the development program of the Interdisciplinary Scientific and Educational School of M. V. Lomonosov Moscow State University “Future Planet and Global Environmental Change”. Authors thank Magee Scientific for AE33 instrumentation support and Dr. Asta Gregorič for data examination. V.O. Kobelev is acknowledged data analyses over all study years....

783 AMAP: AMAP assessment 2015: Black carbon and ozone as Arctic climate forcers, Arctic  
784 Monitoring and Assessment Programme (AMAP), Oslo, Norway, 128 pp. pp., 2015.

785 AMAP: AMAP Arctic Climate Change Update 2021: Key Trends and Impacts,  
786 <https://www.amap.no/documents/download/6759/inline>, 2021.

787 Arnold, S. R., Law, K. S., Brock, C. A., Thomas, J. L., Starkweather, S. M., Von Salzen, K., Stohl,  
788 A., Sharma, S., Lund, M. T., Flanner, M. G., Petäjä, T., Tanimoto, H., Gamble, J., Dibb, J. E.,  
789 Melamed, M., Johnson, N., Fidel, M., Tynkkynen, V. P., Baklanov, A., Eckhardt, S., Monks, S. A.,  
790 Browse, J., and Bozem, H.: Arctic air pollution: Challenges and opportunities for the next decade,  
791 *Elementa*, 2016, 1–17, <https://doi.org/10.12952/journal.elementa.000104>, 2016.

792 Asmi, E., Kivekäs, N., Kerminen, V. M., Komppula, M., Hyvärinen, A. P., Hatakka, J., Viisanen,  
793 Y., and Lihavainen, H.: Secondary new particle formation in Northern Finland Pallas site between  
794 the years 2000 and 2010, *Atmos. Chem. Phys.*, 11, 12959–12972, [https://doi.org/10.5194/acp-11-](https://doi.org/10.5194/acp-11-12959-2011)  
795 12959-2011, 2011.

796 Asmi, E., Backman, J., Servomaa, H., Virkkula, A., Gini, M. I., Eleftheriadis, K., Müller, T., Ohata,  
797 S., Kondo, Y., and Hyvärinen, A.: Absorption instruments inter-comparison campaign at the Arctic  
798 Pallas station, *Atmos. Meas. Tech.*, 14, 5397–5413, <https://doi.org/10.5194/amt-14-5397-2021>,  
799 2021.

800 Backman, J., Schmeisser, L., Virkkula, A., Ogren, J. A., Asmi, E., Starkweather, S., Sharma, S.,  
801 Eleftheriadis, K., Uttal, T., Jefferson, A., Bergin, M., Makshtas, A., Tunved, P., and Fiebig, M.: On  
802 Aethalometer measurement uncertainties and an instrument correction factor for the Arctic, *Atmos.*  
803 *Meas. Tech.*, 10, 5039–5062, <https://doi.org/10.5194/amt-10-5039-2017>, 2017.

804 Bali, K., Banerji, S., Campbell, J. R., Bhakta, A. V., Chen, L. W. A., Holmes, C. D., and Mao, J.:  
805 Measurements of brown carbon and its optical properties from boreal forest fires in Alaska summer,  
806 *Atmos. Environ.*, 324, 120436, <https://doi.org/10.1016/j.atmosenv.2024.120436>, 2024.

807 Bond, T. C., Doherty, S. J., Fahey, D. W., Forster, P. M., Berntsen, T., Deangelo, B. J., Flanner, M.  
808 G., Ghan, S., Kärcher, B., Koch, D., Kinne, S., Kondo, Y., Quinn, P. K., Sarofim, M. C., Schultz,  
809 M. G., Schulz, M., Venkataraman, C., Zhang, H., Zhang, S., Bellouin, N., Guttikunda, S. K.,  
810 Hopke, P. K., Jacobson, M. Z., Kaiser, J. W., Klimont, Z., Lohmann, U., Schwarz, J. P., Shindell,  
811 D., Storelvmo, T., Warren, S. G., and Zender, C. S.: Bounding the role of black carbon in the  
812 climate system: A scientific assessment, *J. Geophys. Res. Atmos.*, 118, 5380–5552,  
813 <https://doi.org/10.1002/jgrd.50171>, 2013.

814 Bondur, V. G., Voronova, O. S., Cherepanova, E. V., Tsidilina, M. N., and Zima, A. L.:  
815 Spatiotemporal Analysis of Multi-Year Wildfires and Emissions of Trace Gases and Aerosols in  
816 Russia Based on Satellite Data, *Izv. - Atmos. Ocean Phys.*, 56, 1457–1469,  
817 <https://doi.org/10.1134/S0001433820120348>, 2020.

818 Böttcher, K., Paunu, V.-V., Kupiainen, K., Zhizhin, M., Matveev, A., Savolahti, M., Klimont, Z.,  
 819 Väättäinen, S., Lamberg, H., and Karvosenoja, N.: Black carbon emissions from flaring in Russia in  
 820 the period 2012-2017, *Atmos. Environ.*, 254, 118390,  
 821 <https://doi.org/10.1016/j.atmosenv.2021.118390>, 2021.  
 822 Bozem, H., Hoor, P., Kunkel, D., Köllner, F., Schneider, J., Herber, A., Schulz, H., Richard  
 823 Leaitch, W., Aliabadi, A. A., Willis, M. D., Burkart, J., and Abbatt, J. P. D.: Characterization of  
 824 transport regimes and the polar dome during Arctic spring and summer using in situ aircraft  
 825 measurements, *Atmos. Chem. Phys.*, 19, 15049–15071, <https://doi.org/10.5194/acp-19-15049-2019>,  
 826 2019.  
 827 Cappa, C. D., Kolesar, K. R., Zhang, X., Atkinson, D. B., Pekour, M. S., Zaveri, R. A., Zelenyuk,  
 828 A., and Zhang, Q.: Understanding the optical properties of ambient sub-and supermicron particulate  
 829 matter: Results from the CARES 2010 field study in northern California, *Atmos. Chem. Phys.*, 16,  
 830 6511–6535, <https://doi.org/10.5194/acp-16-6511-2016>, 2016.  
 831 Cassiani, M., Stohl, A., and Brioude, J.: Lagrangian Stochastic Modelling of Dispersion in the  
 832 Convective Boundary Layer with Skewed Turbulence Conditions and a Vertical Density Gradient:  
 833 Formulation and Implementation in the FLEXPART Model, *Boundary-Layer Meteorol.*, 154, 367–  
 834 390, <https://doi.org/10.1007/s10546-014-9976-5>, 2015.  
 835 Chakrabarty, R. K., Moosmüller, H., Chen, L. W. A., Lewis, K., Arnott, W. P., Mazzoleni, C.,  
 836 Dubey, M. K., Wold, C. E., Hao, W. M., and Kreidenweis, S. M.: Brown carbon in tar balls from  
 837 smoldering biomass combustion, *Atmos. Chem. Phys.*, 10, 6363–6370, <https://doi.org/10.5194/acp-10-6363-2010>, 2010.  
 838  
 839 Chen, X., Kang, S., Yang, J., and Hu, Y.: Contributions of biomass burning in 2019 and 2020 to  
 840 Arctic black carbon and its transport pathways, *Atmos. Res.*, 296, 107069,  
 841 <https://doi.org/10.1016/j.atmosres.2023.107069>, 2023.  
 842 Cuesta-Mosquera, A., Glojek, K., Močnik, G., Drinovec, L., Gregorič, A., Rigler, M., Ogrin, M.,  
 843 Romshoo, B., Weinhold, K., Merkel, M., Van Pinxteren, D., Herrmann, H., Wiedensohler, A.,  
 844 Pöhlker, M., and Müller, T.: Optical properties and simple forcing efficiency of the organic aerosols  
 845 and black carbon emitted by residential wood burning in rural central Europe, *Atmos. Chem. Phys.*,  
 846 24, 2583–2605, <https://doi.org/10.5194/acp-24-2583-2024>, 2024.  
 847 Drinovec, L., Močnik, G., Zotter, P., Prévôt, A. S. H., Ruckstuhl, C., Coz, E., Rupakheti, M.,  
 848 Sciare, J., Müller, T., Wiedensohler, A., and Hansen, A. D. A.: The “dual-spot” Aethalometer: An  
 849 improved measurement of aerosol black carbon with real-time loading compensation, *Atmos. Meas.*  
 850 *Tech.*, 8, 1965–1979, <https://doi.org/10.5194/amt-8-1965-2015>, 2015.  
 851 Eleftheriadis, K., Vratolis, S., and Nyeki, S.: Aerosol black carbon in the European Arctic:  
 852 Measurements at Zeppelin station, Ny-Ålesund, Svalbard from 1998-2007, *Geophys. Res. Lett.*, 36,

1–5, <https://doi.org/10.1029/2008GL035741>, 2009.

Evangelou, N., Balkanski, Y., Hao, W. M., Petkov, A., Silverstein, R. P., Corley, R., Nordgren, B. L., Urbanski, S. P., Eckhardt, S., Stohl, A., Tunved, P., Crepinsek, S., Jefferson, A., Sharma, S., Nøjgaard, J. K., and Skov, H.: Wildfires in northern Eurasia affect the budget of black carbon in the Arctic—a 12-year retrospective synopsis (2002–2013), *Atmos. Chem. Phys.*, 16, <https://doi.org/10.5194/acp-16-7587-2016>, 2016.

Evangelou, N., Platt, S., Eckhardt, S., Lund Myhre, C., Laj, P., Alados-Arboledas, L., Backman, J., Brem, B., Fiebig, M., Flentje, H., Marinoni, A., Pandolfi, M., Yus-Diez, J., Prats, N., Putaud, J., Sellegri, K., Sorribas, M., Eleftheriadis, K., Vratolis, S., Wiedensohler, A., and Stohl, A.: Changes in black carbon emissions over Europe due to COVID-19 lockdowns, *Atmos. Chem. Phys.*, 1–33, <https://doi.org/10.5194/acp-2020-1005>, 2020.

Flanner, M. G.: Arctic climate sensitivity to local black carbon, *J. Geophys. Res. Atmos.*, 118, 1840–1851, <https://doi.org/10.1002/jgrd.50176>, 2013.

Forster, C., Stohl, A., and Seibert, P.: Parameterization of convective transport in a Lagrangian particle dispersion model and its evaluation, *J. Appl. Meteorol. Climatol.*, 46, 403–422, <https://doi.org/10.1175/JAM2470.1>, 2007.

Gilardoni, S., Heslin-Rees, D., Mazzola, M., Vitale, V., Sprenger, M., and Krejci, R.: Drivers controlling black carbon temporal variability in the lower troposphere of the European Arctic, *Atmos. Chem. Phys.*, 23, 15589–15607, <https://doi.org/10.5194/acp-23-15589-2023>, 2023.

Gramlich, Y., Siegel, K., Haslett, S. L., Cremer, R. S., Lunder, C., Kommula, S. M., Buchholz, A., Yttri, K. E., Chen, G., Krejci, R., Zieger, P., Virtanen, A., Riipinen, I., and Mohr, C.: Impact of Biomass Burning on Arctic Aerosol Composition, <https://doi.org/10.1021/acsearthspacechem.3c00187>, 2024.

Grange, S. K., Lötscher, H., Fischer, A., Emmenegger, L., and Hueglin, C.: Evaluation of equivalent black carbon source apportionment using observations from Switzerland between 2008 and 2018, *Atmos. Meas. Tech.*, 13, 1867–1885, <https://doi.org/10.5194/amt-13-1867-2020>, 2020.

Grythe, H., Kristiansen, N. I., Groot Zwaaftink, C. D., Eckhardt, S., Ström, J., Tunved, P., Krejci, R., and Stohl, A.: A new aerosol wet removal scheme for the Lagrangian particle model FLEXPARTv10, *Geosci. Model Dev.*, 10, 1447–1466, <https://doi.org/10.5194/gmd-10-1447-2017>, 2017.

Helin, A., Virkkula, A., Backman, J., Pirjola, L., Sippula, O., Aakko-Saksa, P., Väättäin, S., Mylläri, F., Järvinen, A., Bloss, M., Aurela, M., Jakobi, G., Karjalainen, P., Zimmermann, R., Jokiniemi, J., Saarikoski, S., Tissari, J., Rönkkö, T., Niemä, J. V., and Timonen, H.: Variation of Absorption Ångström Exponent in Aerosols From Different Emission Sources, *J. Geophys. Res. Atmos.*, 126, 1–21, <https://doi.org/10.1029/2020JD034094>, 2021.

888 Hersbach, H., Bell, B., Berrisford, P., Hirahara, S., Horányi, A., Muñoz-Sabater, J., Nicolas, J.,  
 889 Peubey, C., Radu, R., Schepers, D., Simmons, A., Soci, C., Abdalla, S., Abellan, X., Balsamo, G.,  
 890 Bechtold, P., Biavati, G., Bidlot, J., Bonavita, M., De Chiara, G., Dahlgren, P., Dee, D.,  
 891 Diamantakis, M., Dragani, R., Flemming, J., Forbes, R., Fuentes, M., Geer, A., Haimberger, L.,  
 892 Healy, S., Hogan, R. J., Hólm, E., Janisková, M., Keeley, S., Laloyaux, P., Lopez, P., Lupu, C.,  
 893 Radnoti, G., de Rosnay, P., Rozum, I., Vamborg, F., Villaume, S., and Thépaut, J. N.: The ERA5  
 894 global reanalysis, *Q. J. R. Meteorol. Soc.*, 146, 1999–2049, <https://doi.org/10.1002/qj.3803>, 2020.  
 895 Heslin-Rees, D., Burgos, M., Hansson, H. C., Krejci, R., Ström, J., Tunved, P., and Zieger, P.: From  
 896 a polar to a marine environment: Has the changing Arctic led to a shift in aerosol light scattering  
 897 properties?, *Atmos. Chem. Phys.*, 20, 13671–13686, <https://doi.org/10.5194/acp-20-13671-2020>,  
 898 2020.  
 899 Huang, K., Fu, J. S., Prikhodko, V. Y., Storey, J. M., Romanov, A., Hodson, E. L., Cresko, J.,  
 900 Morozova, I., Ignatieva, Y., and Cabaniss, J.: Russian anthropogenic black carbon: Emission  
 901 reconstruction and Arctic black carbon simulation, *J. Geophys. Res. Atmos.*, 120, 11306–11333,  
 902 <https://doi.org/10.1002/2015JD023358>, 2015.  
 903 Ivančič, M., Gregorič, A., Lavrič, G., Alföldy, B., Ježek, I., Hasheminassab, S., Pakbin, P.,  
 904 Ahangar, F., Sowlat, M., Boddeker, S., and Rigler, M.: Two-year-long high-time-resolution  
 905 apportionment of primary and secondary carbonaceous aerosols in the Los Angeles Basin using an  
 906 advanced total carbon–black carbon (TC-BC( $\lambda$ )) method, *Sci. Total Environ.*, 848,  
 907 <https://doi.org/10.1016/j.scitotenv.2022.157606>, 2022.  
 908 Johnson, M. S., Strawbridge, K., Knowland, K. E., Keller, C., and Travis, M.: Long-range transport  
 909 of Siberian biomass burning emissions to North America during FIREX-AQ, *Atmos. Environ.*, 252,  
 910 118241, <https://doi.org/10.1016/j.atmosenv.2021.118241>, 2021.  
 911 Kaiser, J. W., Heil, A., Andreae, M. O., Benedetti, A., Chubarova, N., Jones, L., Morcrette, J. J.,  
 912 Razinger, M., Schultz, M. G., Suttie, M., and Van Der Werf, G. R.: Biomass burning emissions  
 913 estimated with a global fire assimilation system based on observed fire radiative power,  
 914 *Biogeosciences*, 9, 527–554, <https://doi.org/10.5194/bg-9-527-2012>, 2012.  
 915 Kanaya, Y., Komazaki, Y., Pochanart, P., Liu, Y., Akimoto, H., Gao, J., Wang, T., and Wang, Z.:  
 916 Mass concentrations of black carbon measured by four instruments in the middle of Central East  
 917 China in June 2006, *Atmos. Chem. Phys.*, 8, 7637–7649, <https://doi.org/10.5194/acp-8-7637-2008>,  
 918 2008.  
 919 Kasischke, E. S. and Turetsky, M. R.: Recent changes in the fire regime across the North American  
 920 boreal region - Spatial and temporal patterns of burning across Canada and Alaska, *Geophys. Res.*  
 921 *Lett.*, 33, <https://doi.org/10.1029/2006GL025677>, 2006.  
 922 Kharuk, V. I. and Ponomarev, E. I.: Spatiotemporal characteristics of wildfire frequency and

relative area burned in larch-dominated forests of Central Siberia, *Russ. J. Ecol.*, 48, 507–512, <https://doi.org/10.1134/S1067413617060042>, 2017.

Klimont, Z., Kupiainen, K., Heyes, C., Purohit, P., Cofala, J., Rafaj, P., Borken-Kleefeld, J., and Schöpp, W.: Global anthropogenic emissions of particulate matter including black carbon, *Atmos. Chem. Phys.*, 17, 8681–8723, <https://doi.org/10.5194/acp-17-508681-2017>, 2017.

Kostykin, S., Revokatova, A., Chernenkov, A., Ginzburg, V., Polumieva, P., and Zelenova, M.: Black carbon emissions from the siberian fires 2019: Modelling of the atmospheric transport and possible impact on the radiation balance in the arctic region, *Atmosphere (Basel)*, 12, <https://doi.org/10.3390/atmos12070814>, 2021.

Law, K. S. and Stohl, A.: Arctic Air Pollution: Origins and Impacts, *Science (80-. )*, 315, 1537–1540, <https://doi.org/10.1126/science.1137695>, 2007.

Lee, Y. H., Lamarque, J. F., Flanner, M. G., Jiao, C., Shindell, D. T., Berntsen, T., Bisiaux, M. M., Cao, J., Collins, W. J., Curran, M., Edwards, R., Faluvegi, G., Ghan, S., Horowitz, L., McConnell, J. R., Ming, J., Myhre, G., Nagashima, T., Naik, V., Rumbold, S. T., Skeie, R. B., Sudo, K., Takemura, T., Thevenon, F., Xu, B., and Yoon, J. H.: Evaluation of preindustrial to present-day black carbon and its albedo forcing from Atmospheric Chemistry and Climate Model Intercomparison Project (ACCMIP), *Atmos. Chem. Phys.*, 13, 2607–2634, <https://doi.org/10.5194/acp-13-2607-2013>, 2013.

Manousakas, M., Popovicheva, O., Evangeliou, N., Diapouli, E., Sitnikov, N., Shonija, N., and Eleftheriadis, K.: Aerosol carbonaceous, elemental and ionic composition variability and origin at the Siberian High Arctic, Cape Baranova, *Tellus B Chem. Phys. Meteorol.*, 72, 1–14, <https://doi.org/10.1080/16000889.2020.1803708>, 2020.

Markowicz, K. M., Pakszys, P., Ritter, C., Zielinski, T., Udisti, R., Cappelletti, D., Mazzola, M., Shiobara, M., Xian, P., Zawadzka, O., Lisok, J., Petelski, T., Makuch, P., and Karasinski, G.: Impact of North American intense fires on aerosol optical properties measured over the European Arctic in July 2015, *J. Geophys. Res.*, 121, 14487–14512, <https://doi.org/10.1002/2016JD025310>, 2016.

Massling, A., Nielsen, I. E., Kristensen, D., Christensen, J. H., Sorensen, L. L., Jensen, B., Nguyen, Q. T., Nøjgaard, J. K., Glasius, M., and Skov, H.: Atmospheric black carbon and sulfate concentrations in Northeast Greenland, *Atmos. Chem. Phys.*, 15, 9681–9692, <https://doi.org/10.5194/acp-15-9681-2015>, 2015.

Matsui, H., Mori, T., Ohata, S., Moteki, N., Oshima, N., Goto-Azuma, K., Koike, M., and Kondo, Y.: Contrasting source contributions of Arctic black carbon to atmospheric concentrations, deposition flux, and atmospheric and snow radiative effects, *Atmos. Chem. Phys.*, 22, 8989–9009, <https://doi.org/10.5194/acp-22-8989-2022>, 2022.

958 Mokhov, I. I., Bondur, V. G., Sitnov, S. A., and Voronova, O. S.: Satellite Monitoring of Wildfires  
 959 and Emissions into the Atmosphere of Combustion Products in Russia: Relation to Atmospheric  
 960 Blockings, *Dokl. Earth Sci.*, 495, 921–924, <https://doi.org/10.1134/S1028334X20120089>, 2020.

961 Moschos, V., Schmale, J., Aas, W., Becagli, S., Calzolari, G., Eleftheriadis, K., Moffett, C. E.,  
 962 Schnelle-Kreis, J., Severi, M., Sharma, S., Skov, H., Vestenius, M., Zhang, W., Hakola, H., Hellén,  
 963 H., Huang, L., Jaffrezo, J. L., Massling, A., Nøjgaard, J. K., Petäjä, T., Popovicheva, O., Sheesley,  
 964 R. J., Traversi, R., Yttri, K. E., Prévôt, A. S. H., Baltensperger, U., and El Haddad, I.: Elucidating  
 965 the present-day chemical composition, seasonality and source regions of climate-relevant aerosols  
 966 across the Arctic land surface, *Environ. Res. Lett.*, 17, <https://doi.org/10.1088/1748-9326/ac444b>,  
 967 2022a.

968 Moschos, V., Dzepina, K., Bhattu, D., Lamkaddam, H., Casotto, R., Daellenbach, K. R., Canonaco,  
 969 F., Rai, P., Aas, W., Becagli, S., Calzolari, G., Eleftheriadis, K., Moffett, C. E., Schnelle-Kreis, J.,  
 970 Severi, M., Sharma, S., Skov, H., Vestenius, M., Zhang, W., Hakola, H., Hellén, H., Huang, L.,  
 971 Jaffrezo, J. L., Massling, A., Nøjgaard, J. K., Petäjä, T., Popovicheva, O., Sheesley, R. J., Traversi,  
 972 R., Yttri, K. E., Schmale, J., Prévôt, A. S. H., Baltensperger, U., and El Haddad, I.: Equal  
 973 abundance of summertime natural and wintertime anthropogenic Arctic organic aerosols, *Nat.*  
 974 *Geosci.*, 15, 196–202, <https://doi.org/10.1038/s41561-021-00891-1>, 2022b.

975 Ohata, S., Mori, T., Kondo, Y., Sharma, S., Hyvärinen, A., Andrews, E., Tunved, P., Asmi, E.,  
 976 Backman, J., Servomaa, H., Veber, D., Eleftheriadis, K., Vratolis, S., Krejci, R., Zieger, P., Koike,  
 977 M., Kanaya, Y., Yoshida, A., Moteki, N., Zhao, Y., Tobo, Y., Matsushita, J., and Oshima, N.:  
 978 Estimates of mass absorption cross sections of black carbon for filter-based absorption photometers  
 979 in the Arctic, *Atmos. Meas. Tech.*, 14, 6723–6748, <https://doi.org/10.5194/amt-14-6723-2021>,  
 980 2021.

981 Paris, J.-D., Stohl, A., Nédélec, P., Arshinov, M. Y., Panchenko, M. V., Shmargunov, V. P., Law,  
 982 K. S., Belan, B. D., and Ciais, P.: Wildfire smoke in the Siberian Arctic in summer: source  
 983 characterization and plume evolution from airborne measurements, *Atmos. Chem. Phys.*, 9, 9315–  
 984 9327, <https://doi.org/10.5194/acp-9-9315-2009>, 2009, 2009.

985 Petzold, A., Rasp, K., Weinzierl, B., Esselborn, M., Hamburger, T., Dörnbrack, A., Kandler, K.,  
 986 Schütz, L., Knippertz, P., Fiebig, M., and Virkkula, A.: Saharan dust absorption and refractive  
 987 index from aircraft-based observations during SAMUM 2006, *Tellus, Ser. B Chem. Phys.*  
 988 *Meteorol.*, 61, 118–130, <https://doi.org/10.1111/j.1600-0889.2008.00383.x>, 2009.

989 Petzold, A., Ogren, J. A., Fiebig, M., Laj, P., Li, S. M., Baltensperger, U., Holzer-Popp, T., Kinne,  
 990 S., Pappalardo, G., Sugimoto, N., Wehrli, C., Wiedensohler, A., and Zhang, X. Y.:  
 991 Recommendations for reporting black carbon measurements, *Atmos. Chem. Phys.*, 13, 8365–8379,  
 992 <https://doi.org/10.5194/acp-13-8365-2013>, 2013.



993 Piss0, I., Sollum, E., Grythe, H., Kristiansen, N. I., Cassiani, M., Eckhardt, S., Arnold, D., Morton,  
 994 D., Thompson, R. L., Groot Zwaafink, C. D., Evangeliou, N., Sodemann, H., Haimberger, L.,  
 995 Henne, S., Brunner, D., Burkhardt, J. F., Fouilloux, A., Brioude, J., Philipp, A., Seibert, P., and  
 996 Stohl, A.: The Lagrangian particle dispersion model FLEXPART version 10.4, *Geosci. Model Dev.*,  
 997 12, 4955–4997, <https://doi.org/10.5194/gmd-12-4955-2019>, 2019.  
 998 Platt, S., Hov, Ø., Berg, T., Breivik, K., Eckhardt, S., Eleftheriadis, K., Evangeliou, N., Fiebig, M.,  
 999 Fisher, R., Hansen, G., Hansson, H.-C., Heintzenberg, J., Hermansen, O., Heslin-Rees, D., Holmén,  
 1000 K., Hudson, S., Kallenborn, R., Krejci, R., Krognes, T., Larssen, S., Lowry, D., Lund Myhre, C.,  
 1001 Lunder, C., Nisbet, E., Nizetto, P., Park, K.-T., Pedersen, C., Aspmo Pfaffhuber, K., Röckmann, T.,  
 1002 Schmidbauer, N., Solberg, S., Stohl, A., Ström, J., Svendby, T., Tunved, P., Tørnkqvist, K., van der  
 1003 Veen, C., Vratolis, S., Yoon, Y. J., Yttri, K. E., Zieger, P., Aas, W., and Tørseth, K.: Atmospheric  
 1004 composition in the European Arctic and 30 years of the Zeppelin Observatory, Ny-Ålesund, *Atmos.*  
 1005 *Chem. Phys.*, 1–80, 2021.  
 1006 Popovicheva, O., Diapouli, E., Makshtas, A., Shonija, N., Manousakas, M., Saraga, D., Uttal, T.,  
 1007 and Eleftheriadis, K.: East Siberian Arctic background and black carbon polluted aerosols at HMO  
 1008 Tiksi, *Sci. Total Environ.*, 655, 924–938, <https://doi.org/10.1016/j.scitotenv.2018.11.165>, 2019a.  
 1009 Popovicheva, O. B., Shonija, N. K., Persiantseva, N., Timofeev, M., Diapouli, E., Eleftheriadis, K.,  
 1010 Borgese, L., and Nguyen, X. A.: Aerosol pollutants during agricultural biomass burning: A case  
 1011 study in Ba Vi Region in Hanoi, Vietnam, *Aerosol Air Qual. Res.*, 17, 2762–2779,  
 1012 <https://doi.org/10.4209/aaqr.2017.03.0111>, 2017a.  
 1013 Popovicheva, O. B., Evangeliou, N., Eleftheriadis, K., Kalogridis, A. C., Sitnikov, N., Eckhardt, S.,  
 1014 and Stohl, A.: Black Carbon Sources Constrained by Observations in the Russian High Arctic,  
 1015 *Environ. Sci. Technol.*, 51, <https://doi.org/10.1021/acs.est.6b05832>, 2017b.  
 1016 Popovicheva, O. B., Engling, G., Ku, I. T., Timofeev, M. A., and Shonija, N. K.: Aerosol emissions  
 1017 from long-lasting smoldering of boreal peatlands: Chemical composition, markers, and  
 1018 microstructure, *Aerosol Air Qual. Res.*, 19, 484–503, <https://doi.org/10.4209/aaqr.2018.08.0302>,  
 1019 2019b.  
 1020 Popovicheva, O. B., Evangeliou, N., Kobelev, V. O., Chichaeva, M. A., Eleftheriadis, K., Gregorič,  
 1021 A., and Kasimov, N. S.: Siberian Arctic black carbon: gas flaring and wildfire impact, *Atmos.*  
 1022 *Chem. Phys.*, 22, 5983–6000, <https://doi.org/10.5194/acp-22-5983-2022>, 2022.  
 1023 Popovicheva, O. B., Chichaeva, M. A., Kobelev, V. O., and Kasimov, N. S.: Black Carbon  
 1024 Seasonal Trends and Regional Sources on Bely Island (Arctic), *Atmos. Ocean. Opt.*, 36, 176–184,  
 1025 <https://doi.org/10.1134/S1024856023030090>, 2023.  
 1026 Pulimeno, S., Bruschi, F., Feltracco, M., Mazzola, M., Gilardoni, S., Crocchianti, S., Cappelletti,  
 1027 D., Gambaro, A., and Barbaro, E.: Investigating the Presence of Biomass Burning Events at Ny-Å

1028 Lesund: Optical and Chemical Insights from Summer-Fall 2019, *Atmos. Environ.*, 320, 120336,  
 1029 <https://doi.org/10.1016/j.atmosenv.2024.120336>, 2024.  
 1030 Qi, L. and Wang, S.: Sources of black carbon in the atmosphere and in snow in the Arctic, *Sci.*  
 1031 *Total Environ.*, 691, 442–454, <https://doi.org/10.1016/j.scitotenv.2019.07.073>, 2019.  
 1032 Ran, L., Deng, Z. Z., Wang, P. C., and Xia, X. A.: Black carbon and wavelength-dependent aerosol  
 1033 absorption in the North China Plain based on two-year aethalometer measurements, *Atmos.*  
 1034 *Environ.*, 142, 132–144, <https://doi.org/10.1016/j.atmosenv.2016.07.014>, 2016.  
 1035 Rogers, B. M., Balch, J. K., Goetz, S. J., Lehmann, C. E. R., and Turetsky, M.: Focus on changing  
 1036 fire regimes: interactions with climate, ecosystems, and society, *Environ. Res. Lett.*, 15,  
 1037 <https://doi.org/10.1088/1748-9326/ab6d3a>, 2020.  
 1038 Sandradewi, J., Prévôt, A. S. H., Szidat, S., Perron, N., Alfarra, M. R., Lanz, V. A., Weingartner,  
 1039 E., and Baltensperger, U. R. S.: Using aerosol light absorption measurements for the quantitative  
 1040 determination of wood burning and traffic emission contribution to particulate matter, *Environ. Sci.*  
 1041 *Technol.*, 42, 3316–3323, <https://doi.org/10.1021/es702253m>, 2008.  
 1042 Schmale, J., Zieger, P., and Ekman, A. M. L.: Aerosols in current and future Arctic climate, *Nat.*  
 1043 *Clim. Chang.*, 11, 95–105, <https://doi.org/10.1038/s41558-020-00969-5>, 2021.  
 1044 Schmale, J., Sharma, S., Decesari, S., Pernov, J., Massling, A., Hansson, H. C., Von Salzen, K.,  
 1045 Skov, H., Andrews, E., Quinn, P. K., Upchurch, L. M., Eleftheriadis, K., Traversi, R., Gilardoni, S.,  
 1046 Mazzola, M., Laing, J., and Hopke, P.: Pan-Arctic seasonal cycles and long-term trends of aerosol  
 1047 properties from 10 observatories, *Atmos. Chem. Phys.*, 22, 3067–3096, [https://doi.org/10.5194/acp-](https://doi.org/10.5194/acp-22-3067-2022)  
 1048 [22-3067-2022](https://doi.org/10.5194/acp-22-3067-2022), 2022.  
 1049 Schmeisser, L., Backman, J., Ogren, J. A., Andrews, E., Asmi, E., Starkweather, S., Uttal, T.,  
 1050 Fiebig, M., Sharma, S., Eleftheriadis, K., Vratolis, S., Bergin, M., Tunved, P., and Jefferson, A.:  
 1051 Seasonality of aerosol optical properties in the Arctic, *Atmos. Chem. Phys.*, 18, 11599–11622,  
 1052 <https://doi.org/10.5194/acp-18-11599-2018>, 2018.  
 1053 Schneider, E., Czech, H., Popovicheva, O., Chichaeva, M., Kobelev, V., Kasimov, N., Minkina, T.,  
 1054 Rüger, C. P., and Zimmermann, R.: Mass spectrometric analysis of unprecedented high levels of  
 1055 carbonaceous aerosol particles long-range transported from wildfires in the Siberian Arctic, *Atmos.*  
 1056 *Chem. Phys.*, 24, 553–576, <https://doi.org/10.5194/acp-24-553-2024>, 2024.  
 1057 Sharma, S., Lavoué, D., Chachier, H., Barrie, L. A., and Gong, S. L.: Long-term trends of the black  
 1058 carbon concentrations in the Canadian Arctic, *J. Geophys. Res. D Atmos.*, 109, 1–10,  
 1059 <https://doi.org/10.1029/2003JD004331>, 2004.  
 1060 Sharma, S., Ishizawa, M., Chan, D., Lavoué, D., Andrews, E., Eleftheriadis, K., and Maksyutov, S.:  
 1061 16-year simulation of arctic black carbon: Transport, source contribution, and sensitivity analysis on  
 1062 deposition, *J. Geophys. Res. Atmos.*, 118, 943–964, <https://doi.org/10.1029/2012JD017774>, 2013.

1063 Sharma, S., Richard Leaitch, W., Huang, L., Veber, D., Kolonjari, F., Zhang, W., Hanna, S. J.,  
 1064 Bertram, A. K., and Ogren, J. A.: An evaluation of three methods for measuring black carbon in  
 1065 Alert, Canada, *Atmos. Chem. Phys.*, 17, 15225–15243, <https://doi.org/10.5194/acp-17-15225-2017>,  
 1066 2017.  
 1067 Silver, B., Arnold, S. R., Reddington, C. L., Emmons, L. K., and Conibear, L.: Large transboundary  
 1068 health impact of Arctic wildfire smoke, *Commun. Earth Environ.*, 5,  
 1069 <https://doi.org/10.1038/s43247-024-01361-3>, 2024.  
 1070 Singh, M., Kondo, Y., Ohata, S., Mori, T., Oshima, N., Hyvärinen, A., Backman, J., Asmi, E.,  
 1071 Servomaa, H., Schnaiter, F. M., Andrews, E., Sharma, S., Eleftheriadis, K., Vratolis, S., Zhao, Y.,  
 1072 Koike, M., Moteki, N., and Sinha, P. R.: Mass absorption cross section of black carbon for  
 1073 Aethalometer in the Arctic, *Aerosol Sci. Technol.*, 58, 536–553,  
 1074 <https://doi.org/10.1080/02786826.2024.2316173>, 2024.  
 1075 Stathopoulos, V. K., Evangeliou, N., Stohl, A., Vratolis, S., Matsoukas, C., and Eleftheriadis, K.:  
 1076 Large Circulation Patterns Strongly Modulate Long-Term Variability of Arctic Black Carbon  
 1077 Levels and Areas of Origin, *Geophys. Res. Lett.*, 48, 1–10, <https://doi.org/10.1029/2021GL092876>,  
 1078 2021.  
 1079 Stohl, A.: Characteristics of atmospheric transport into the Arctic troposphere, *J. Geophys. Res.*  
 1080 *Atmos.*, 111, 1–17, <https://doi.org/10.1029/2005JD006888>, 2006.  
 1081 Stohl, A., Forster, C., Frank, A., Seibert, P., and Wotawa, G.: Technical note: The Lagrangian  
 1082 particle dispersion model FLEXPART version 6.2, *Atmos. Chem. Phys.*, 5, 2461–2474,  
 1083 <https://doi.org/10.5194/acp-5-2461-2005>, 2005.  
 1084 Stohl, A., Klimont, Z., Eckhardt, S., Kupiainen, K., Shevchenko, V. P., Kopeikin, V. M., and  
 1085 Novigatsky, A. N.: Black carbon in the Arctic: The underestimated role of gas flaring and  
 1086 residential combustion emissions, *Atmos. Chem. Phys.*, 13, 8833–8855,  
 1087 <https://doi.org/10.5194/acp-13-8833-2013>, 2013.  
 1088 Stone, R. S., Sharma, S., Herber, A., Eleftheriadis, K., and Nelson, D. W.: A characterization of  
 1089 Arctic aerosols on the basis of aerosol optical depth and black carbon measurements, *Elem. Sci.*  
 1090 *Anthr.*, 2, 1–22, <https://doi.org/10.12952/journal.elementa.000027>, 2014.  
 1091 Therneau, T.: deming: Deming, Theil-Sen, Passing-Bablok and Total Least Squares Regression,  
 1092 2024.  
 1093 Tomshin, O. and Solovyev, V.: Features of the Extreme Fire Season of 2021 in Yakutia (Eastern  
 1094 Siberia) and Heavy Air Pollution Caused by Biomass Burning, *Remote Sens.*, 14,  
 1095 <https://doi.org/10.3390/rs14194980>, 2022.  
 1096 Tunved, P., Ström, J., and Krejci, R.: Arctic aerosol life cycle: Linking aerosol size distributions  
 1097 observed between 2000 and 2010 with air mass transport and precipitation at Zeppelin station, Ny-

1098 Ålesund, Svalbard, *Atmos. Chem. Phys.*, 13, 3643–3660, [https://doi.org/10.5194/acp-13-3643-](https://doi.org/10.5194/acp-13-3643-2013)  
 1099 2013, 2013.

1100 Ulevicius, V., Byčenkienė, S., Remeikis, V., Garbaras, A., Kecorius, S., Andriejauskienė, J.,  
 1101 Jasinevičienė, D., and Mocnik, G.: Characterization of pollution events in the East Baltic region  
 1102 affected by regional biomass fire emissions, *Atmos. Res.*, 98, 190–200,  
 1103 <https://doi.org/10.1016/j.atmosres.2010.03.021>, 2010.

1104 Veraverbeke, S., Rogers, B. M., Goulden, M. L., Jandt, R. R., Miller, C. E., Wiggins, E. B., and  
 1105 Randerson, J. T.: Lightning as a major driver of recent large fire years in North American boreal  
 1106 forests, *Nat. Clim. Chang.*, 7, 529–534, <https://doi.org/10.1038/nclimate3329>, 2017.

1107 Vinogradova, A. A. and Ivanova, Y. A.: Atmospheric Transport of Black Carbon to the Russian  
 1108 Arctic from Different Sources: Winter and Summer 2000–2016, *Atmos. Ocean. Opt.*, 36, 758–766,  
 1109 <https://doi.org/10.1134/S1024856023060222>, 2023.

1110 Virkkula, A.: Modeled source apportionment of black carbon particles coated with a light-scattering  
 1111 shell, *Atmos. Meas. Tech.*, 14, 3707–3719, <https://doi.org/10.5194/amt-14-3707-2021>, 2021.

1112 Voronova, O. S., Zima, A. L., Kladov, V. L., and Cherepanova, E. V.: Anomalous Wildfires in  
 1113 Siberia in Summer 2019, *Izv. - Atmos. Ocean Phys.*, 56, 1042–1052,  
 1114 <https://doi.org/10.1134/S000143382009025X>, 2020.

1115 Voronova, O. S., Gordo, K. A., Zima, A. L., and Feoktistova, N. V.: Strong Wildfires in the  
 1116 Russian Federation in 2021 Detected Using Satellite Data, *Izv. - Atmos. Ocean Phys.*, 58, 1065–  
 1117 1076, <https://doi.org/10.1134/S0001433822090225>, 2022.

1118 Willis, M. D., Leaitch, W. R., and Abbatt, J. P. D.: Processes Controlling the Composition and  
 1119 Abundance of Arctic Aerosol, *Rev. Geophys.*, 56, 621–671,  
 1120 <https://doi.org/10.1029/2018RG000602>, 2018.

1121 Winiger, P., Andersson, A., Eckhardt, S., Stohl, A., Semiletov, I. P., Dudarev, O. V., Charkin, A.,  
 1122 Shakhova, N., Klimont, Z., Heyes, C., and Gustafsson, Ö.: Siberian Arctic black carbon sources  
 1123 constrained by model and observation, *Proc. Natl. Acad. Sci.*, 114, E1054–E1061,  
 1124 <https://doi.org/10.1073/pnas.1613401114>, 2017.

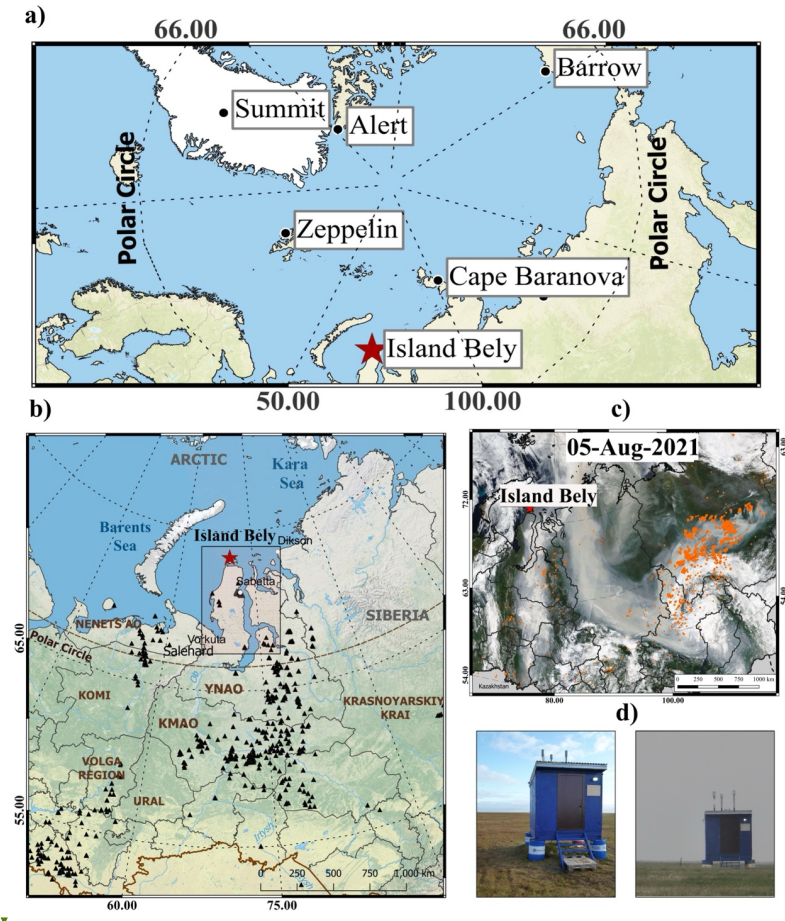
1125 Winiger, P., Barrett, T. E., Sheesley, R. J., Huang, L., Sharma, S., Barrie, L. A., and Yttri, K. E.:  
 1126 Source apportionment of circum-Arctic atmospheric black carbon from isotopes and modeling, *Sci.*  
 1127 *Adv.*, 5, eaau8052, <https://doi.org/10.1126/sciadv.aau8052>, 2019.

1128 Yttri, K. E., Lund Myhre, C., Eckhardt, S., Fiebig, M., Dye, C., Hirdman, D., Ström, J., Klimont,  
 1129 Z., and Stohl, A.: Quantifying black carbon from biomass burning by means of levoglucosan - A  
 1130 one-year time series at the Arctic observatory Zeppelin, *Atmos. Chem. Phys.*, 14, 6427–6442,  
 1131 <https://doi.org/10.5194/acp-14-6427-2014>, 2014.

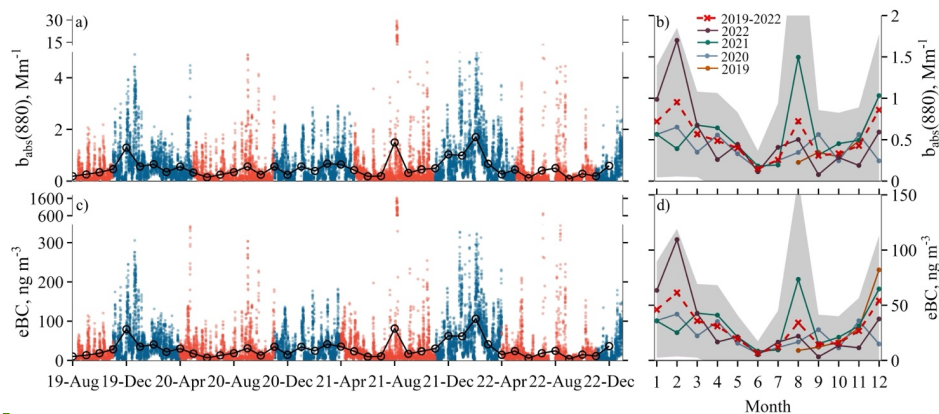
1132 Yttri, K. E., Bäcklund, A., Conen, F., Eckhardt, S., Evangeliou, N., Fiebig, M., Kasper-Giebl, A.,

1133 Gold, A., Gundersen, H., Myhre, C. L., Platt, S. M., Simpson, D., Surratt, J. D., Szidat, S., Rauber,  
 1134 M., Torseth, K., Ytre-Eide, M. A., Zhang, Z., and Aas, W.: Composition and sources of  
 1135 carbonaceous aerosol in the European Arctic at Zeppelin Observatory, Svalbard, *Atmos. Chem.*  
 1136 *Phys.*, 24, 2731–2758, 2024.  
 1137 Yue, S., Zhu, J., Chen, S., Xie, Q., Li, W., Li, L., Ren, H., Su, S., Li, P., Ma, H., Fan, Y., Cheng, B.,  
 1138 Wu, L., Deng, J., Hu, W., Ren, L., Wei, L., Zhao, W., Tian, Y., Pan, X., Sun, Y., Wang, Z., Wu, F.,  
 1139 Liu, C. Q., Su, H., Penner, J. E., Pöschl, U., Andreae, M. O., Cheng, Y., and Fu, P.: Brown carbon  
 1140 from biomass burning imposes strong circum-Arctic warming, *One Earth*, 5, 293–304,  
 1141 <https://doi.org/10.1016/j.oneear.2022.02.006>, 2022.  
 1142 Zanatta, M., Laj, P., Gysel, M., Baltensperger, U., Vratolis, S., Eleftheriadis, K., Kondo, Y.,  
 1143 Dubuisson, P., Winiarek, V., Kazadzis, S., Tunved, P., and Jacobi, H. W.: Effects of mixing state on  
 1144 optical and radiative properties of black carbon in the European Arctic, *Atmos. Chem. Phys.*, 18,  
 1145 14037–14057, <https://doi.org/10.5194/acp-18-14037-2018>, 2018.  
 1146 Zenkova, P. N., Chernov, D. G., Shmargunov, V. P., Panchenko, M. V., and Belan, B. D.:  
 1147 Submicron Aerosol and Absorbing Substance in the Troposphere of the Russian Sector of the Arctic  
 1148 According to Measurements Onboard the Tu-134 Optik Aircraft Laboratory in 2020, *Atmos. Ocean.*  
 1149 *Opt.*, 35, 43–51, <https://doi.org/10.1134/S1024856022010146>, 2022.  
 1150 Zhou, C., Penner, J. E., Flanner, M. G., Bisiaux, M. M., Edwards, R., and McConnell, J. R.:  
 1151 Transport of black carbon to polar regions: Sensitivity and forcing by black carbon, *Geophys. Res.*  
 1152 *Lett.*, 39, 1–6, <https://doi.org/10.1029/2012GL053388>, 2012.  
 1153 Zhu, C., Kanaya, Y., Takigawa, M., Ikeda, K., Tanimoto, H., Taketani, F., Miyakawa, T.,  
 1154 Kobayashi, H., and Pissu, I.: FLEXPART v10.1 simulation of source contributions to Arctic black  
 1155 carbon, *Atmos. Chem. Phys.*, 20, 1641–1656, <https://doi.org/10.5194/acp-20-1641-2020>, 2020.  
 1156  
 1157

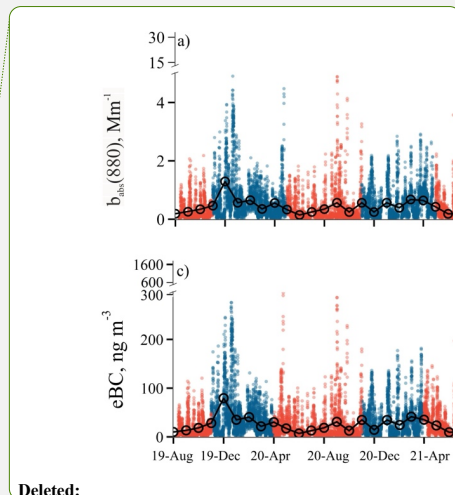
1160  
1161  
1162  
1163  
1164  
1165  
1166  
1167  
1168  
1169  
1170  
1171  
1172  
1173  
1174

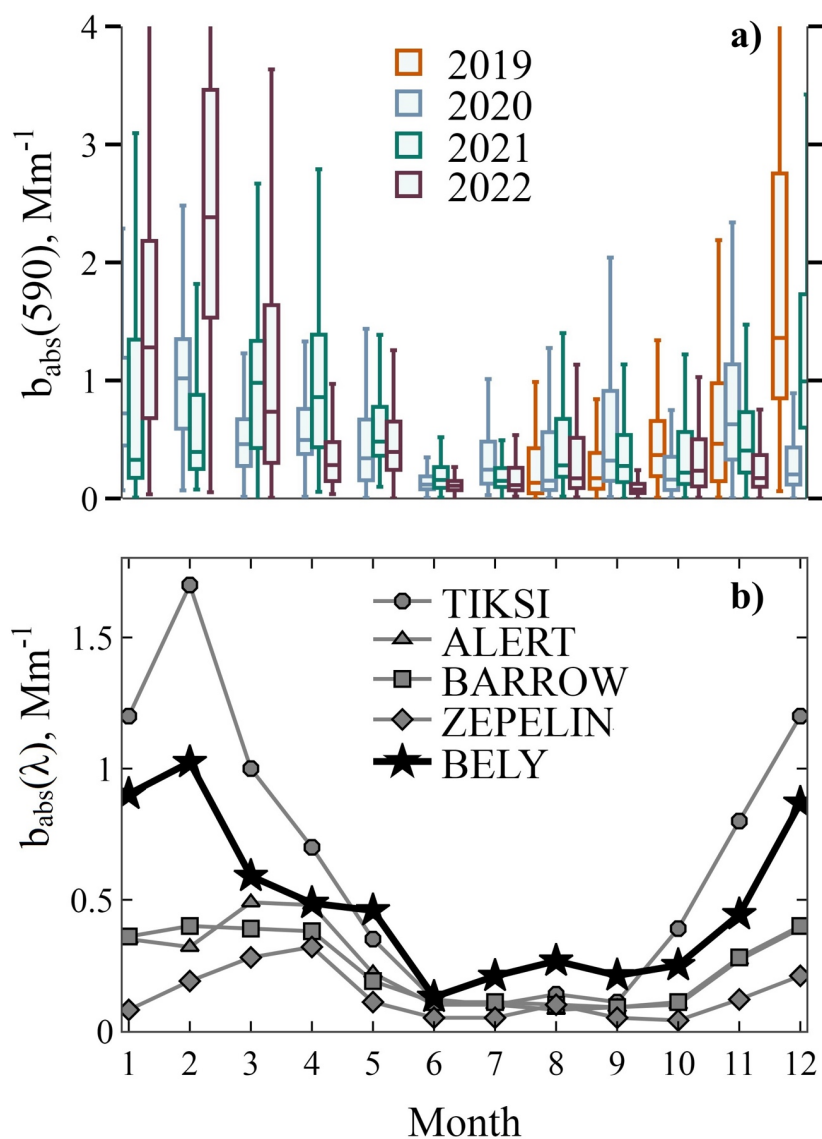


**Figure 1.** (a) The IBS between other polar aerosol stations. (b) A map showing IBS in Western Siberia along with oil and gas fields (adopted from <https://skytruth.org/>, last access: 7 November 2024). Flares of oil and gas fields are indicated for 2020 as black triangles (<https://skytruth.org/>, last access: 7 November 2024). (c) Satellite image of strong plume from the area of Yakutian wildfires which brought deep smoke to the Bely Island. (d) View to the pavilion of IBS under clear conditions on 25 July 2021, and during the unprecedented smoke event on 5 August 2021. Maps were created using Open-Source Geographic Information System QGIS (<https://qgis.org/en/site>, last access: 7 November 2024) with ESRI physical imagery ([https://server.arcgisonline.com/ArcGIS/rest/services/World\\_Physical\\_Map/MapServer/tile/%7Bz%7D/%7By%7D/%7Bx%7D&zmax=20&zmin=0](https://server.arcgisonline.com/ArcGIS/rest/services/World_Physical_Map/MapServer/tile/%7Bz%7D/%7By%7D/%7Bx%7D&zmax=20&zmin=0), last access: 7 November 2024) as the base layer, and for MODIS Reflectance true color imagery (MODIS Science Team) and Satellite imagery from 05 of August 2021 (<https://worldview.earthdata.nasa.gov>, last access: 7 November 2024) with TERRA MODIS fire anomaly layer. Open-source Natural Earth quick start (NEQS) package was used to add layers of natural and cultural boundaries and polygons from ESRI Shapefile storage.

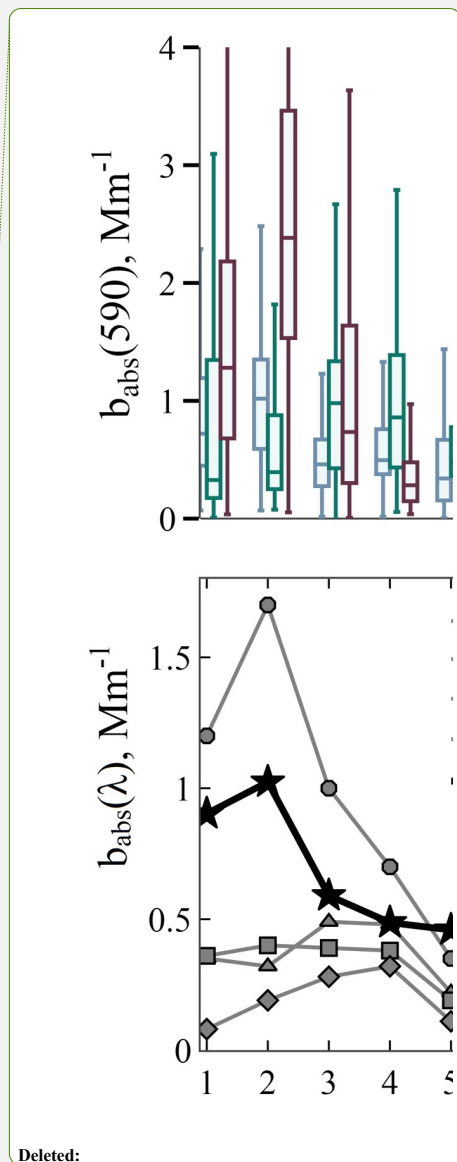


**Figure 2.** Hourly timeseries and monthly means of (a)  $b_{abs}(880)$  and (c)  $eBC$  for cold (blue) and warm (red) periods; monthly climatology of (b)  $b_{abs}(880)$  and (d)  $eBC$  for half year 2019 and 2020, 2021, and 2022. Cross-marks (x) joined by lines show the inter-annual mean; the standard deviation is plotted by shadow area.





**Figure 3.** (a) Monthly box-whisker plot for  $b_{abs}(590)$  at IBS for half year 2019 and full 2020, 2021, and 2022. The 25<sup>th</sup>, 50<sup>th</sup>, and 75<sup>th</sup> percentiles are shown with boxes, while whiskers extend  $\pm 1.5$  times the interquartile range. (b) Seasonality of monthly median of  $b_{abs}$  at 550 nm at Tiksi, Alert, Barrow/Utqiagvik, Zepelin for 2012-2014 (Schmeisser et al., 2018), and  $b_{abs}$  at 590 nm at IBS for 2019-2022 (this work).





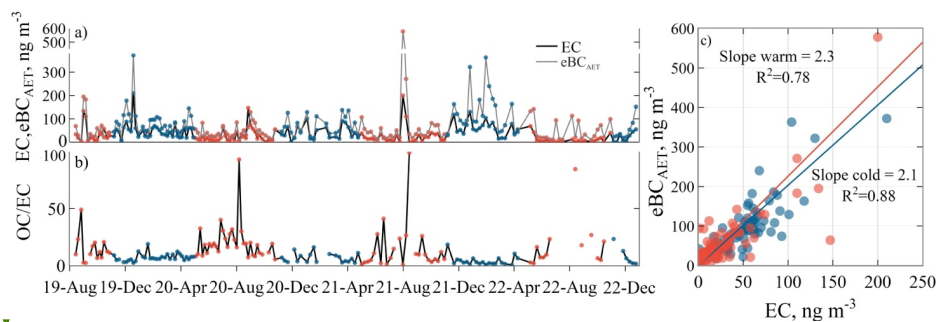
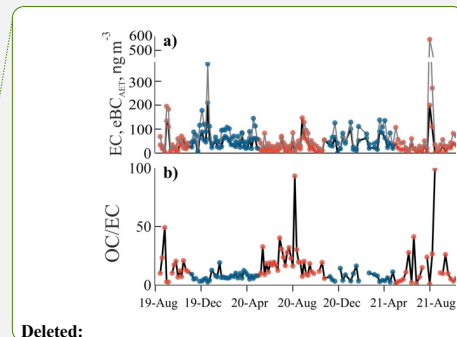


**Figure 4.** Temporal variation of (a) weekly EC and  $eBC_{AET}$  averaged over the whole sampling period and (b) the OC/EC ratio. (c) Scatter plots and orthogonal regressions (solid lines) for measured  $eBC_{AET}$  and EC concentrations in cold (blue) and warm (red) period. The figure includes the regression slope, the coefficient of determination ( $R^2$ ).



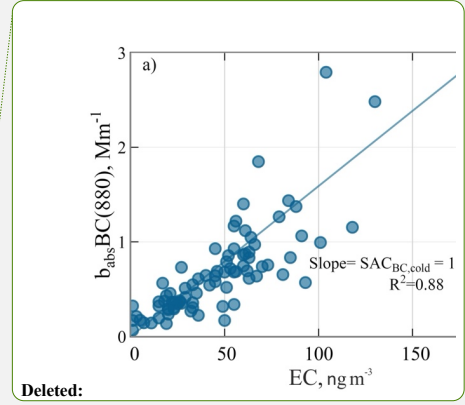
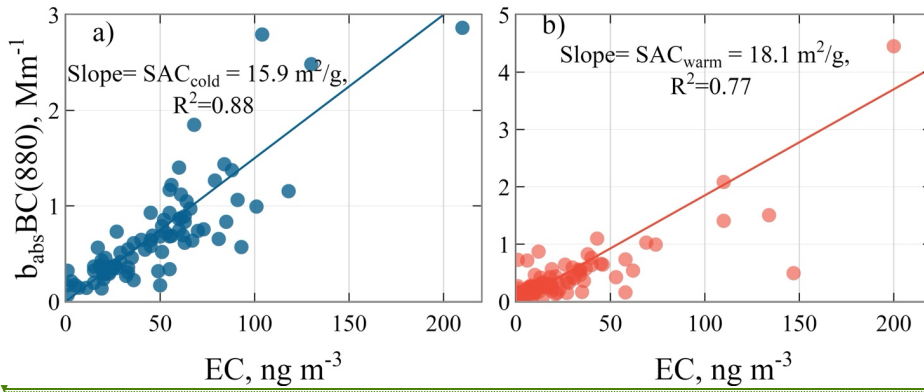
1199

1200

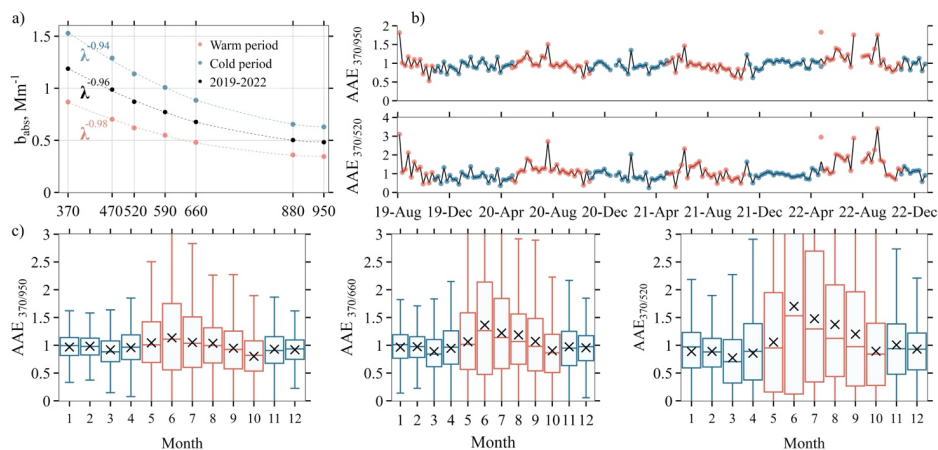
1201 **Figure 5.** Scatter plots and orthogonal regressions (solid line) for  $b_{abs/BC}(880)$  and EC  
 1202 concentrations for the (a) cold (blue) and (b) warm (red) periods. Regression slope defines  
 1203  $SAC_{BC,cold}$  and  $SAC_{BC,warm}$ .

1204

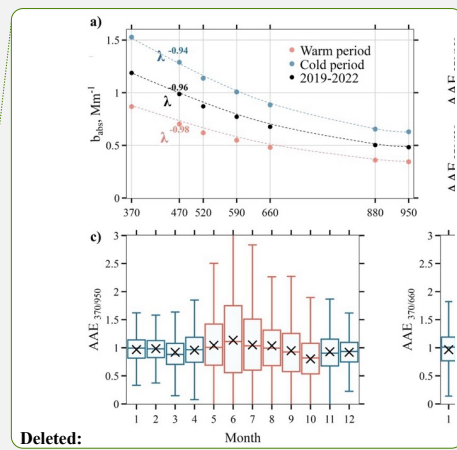
1205



Deleted:



**Figure 6.** (a) Spectral dependence of light absorption coefficient for 2019-2022, during warm (red) and cold (blue) periods.  $AAE_{350/950}$  is the slope of the linear regression in logarithmic scale of a power law regression as described in Eq. 2. (b) Timeseries of  $AAE_{370/950}$  and  $AAE_{370/520}$ . (c) Box-whisker plots and monthly means of  $AAE$  at 370 and 950 nm, 370 and 660 nm, and 370 and 520 nm for the entire period.



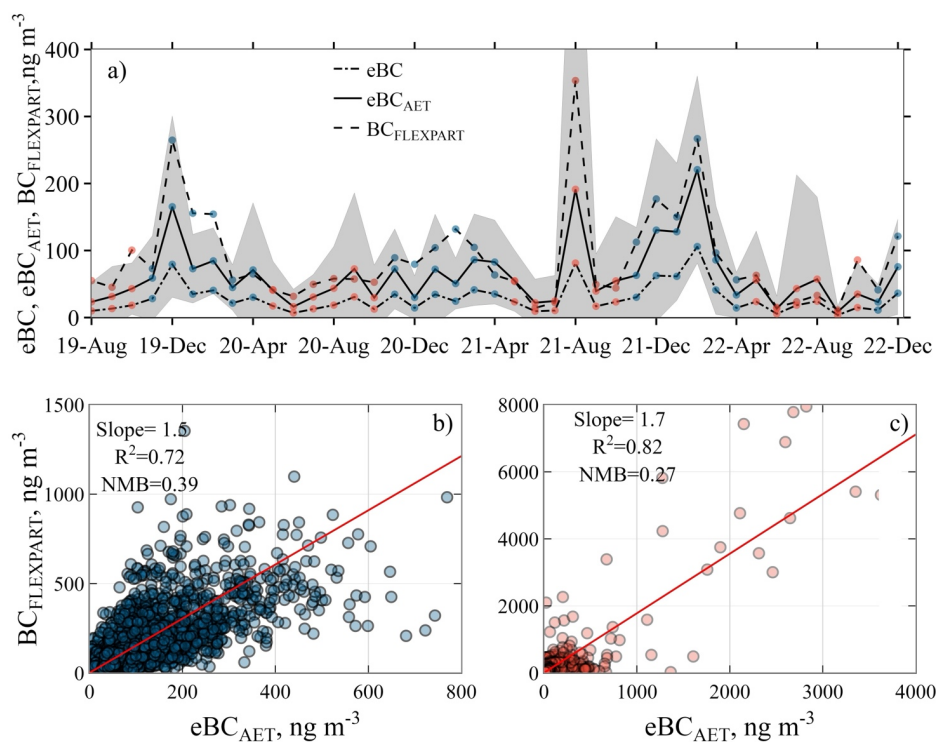
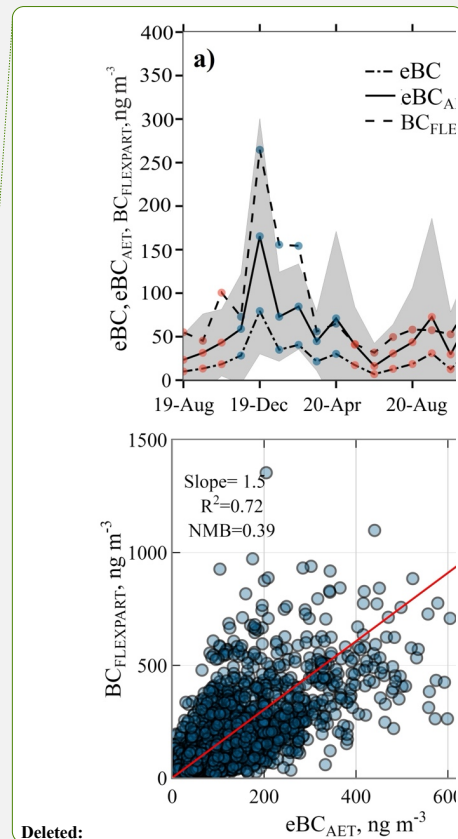


**Figure 7.** (a) Monthly mean  $eBC$  and modelled surface BC concentrations from 10 August 2019 to 31 December 2022. Monthly mean  $eBC_{AET}$  (line with crosses) shown with the standard deviation range by shadowed area. Scatter plots and orthogonal regressions (solid lines) for  $BC_{FLEXPART}$  calculated over measured  $eBC_{AET}$  concentrations for (b) cold and (c) warm period. The figure includes the regression slope, the coefficient of determination ( $R^2$ ).



Deleted:

# VERTICAL CROSS-SECTIONS OF MODELLED BC IN IBS

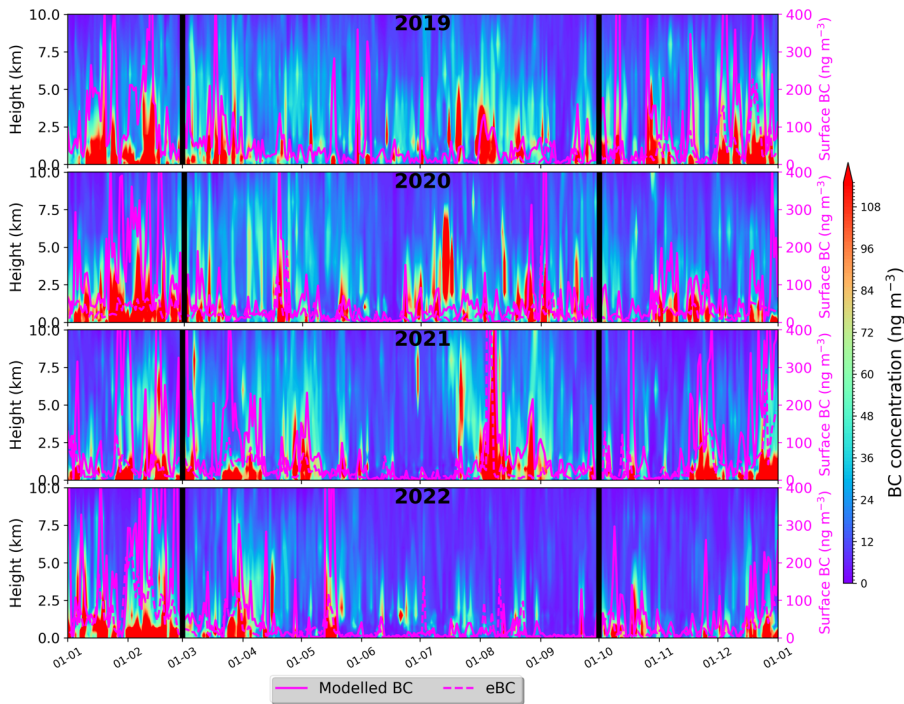
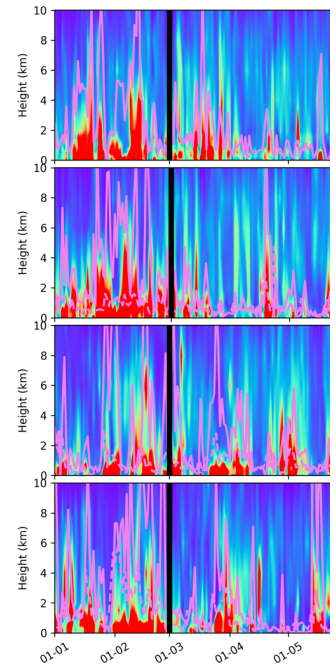


**Figure 8.** Vertical cross-sections of modelled BC for 2019-2022. Solid and dotted lines represent modelled daily surface BC and *eBC*, respectively. Their levels correspond to the right (secondary) axis (also in gray). Boundaries between the cold (November- April) and warm (May- October) are indicated by thick vertical black lines.

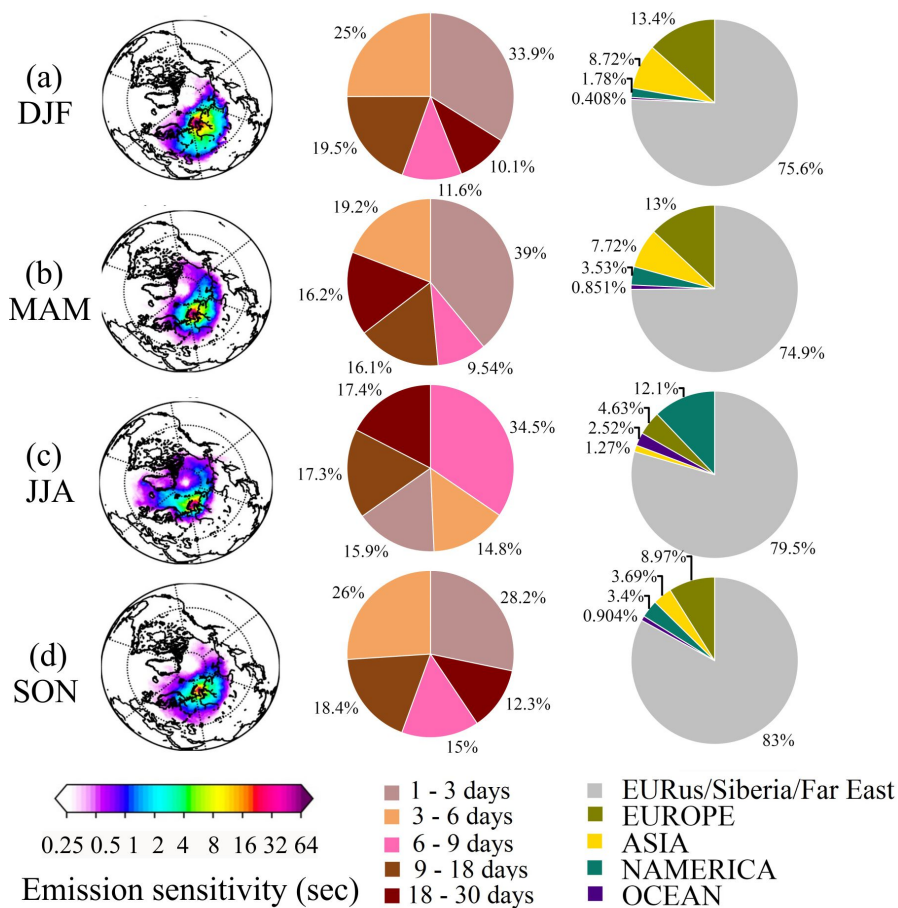
## VERTICAL CRO:



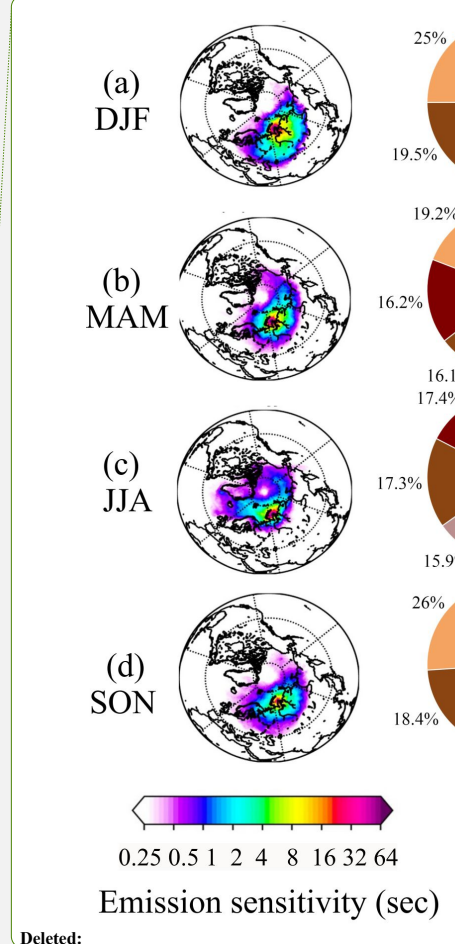
Deleted:

Deleted: violet

Deleted: violet



**Figure 9.** (a-d) Season average footprint emission sensitivity, mean age contribution of emissions from different day-periods back in time and each region contribution to surface concentration of BC.





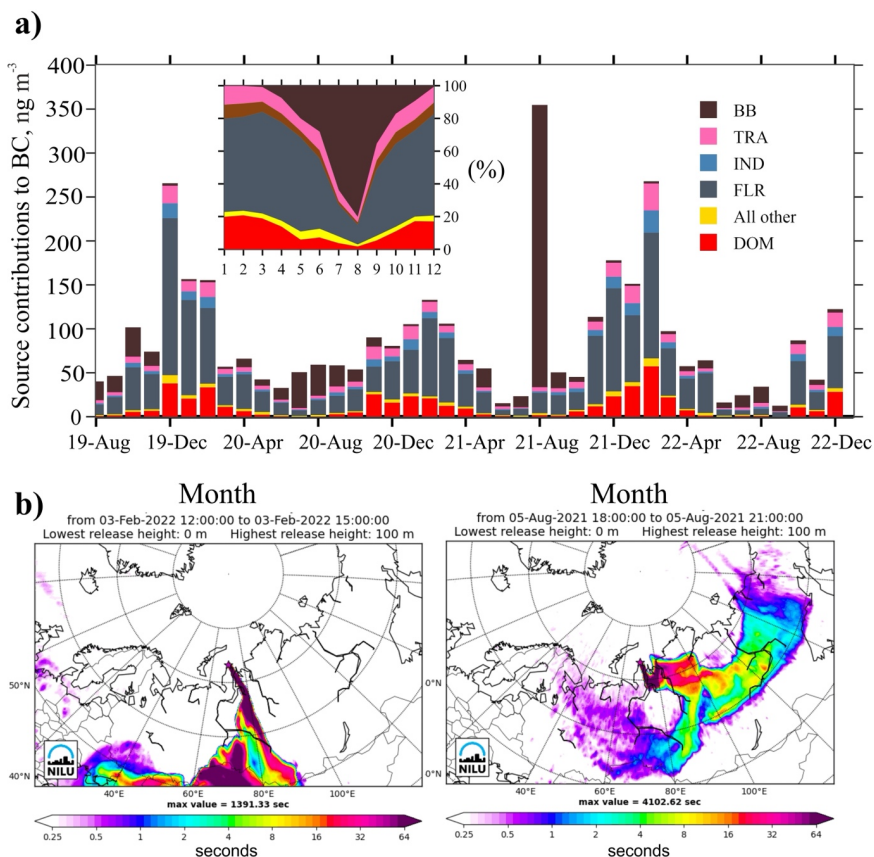
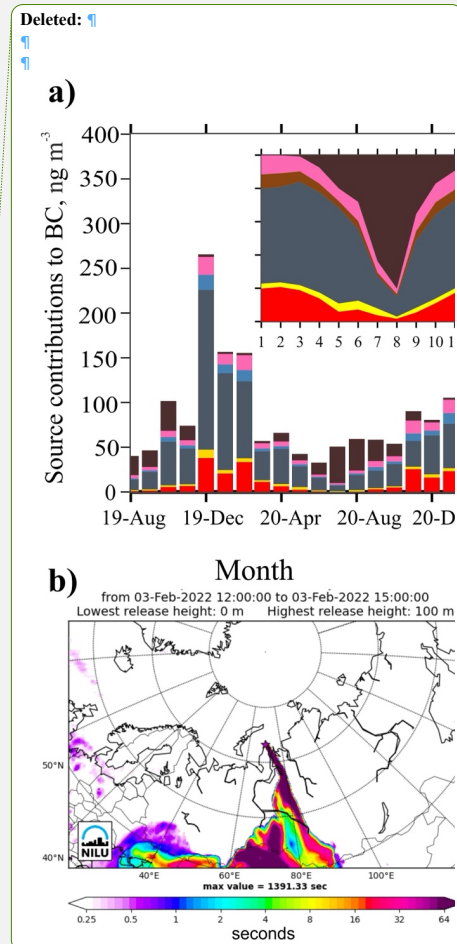


**Figure 10.** (a) Timeseries of monthly mean contribution from different emission source types to surface BC concentrations for the study period. DOM, BB, TRA, IND, FLR sectors, and All others sources were adopted from ECLIPSEv6 and CAMS GFAS. (b) FES for 3 February 2022 and 5 August 2021 showing the largest probability of emission origin.



1248 **TABLES & LEGENDS**

1249

1250

1251 **Table 1.** Statistics of light - absorption coefficients; EC, OC,  $eBC_{AET}$ , and  $eBC$  mass concentration;  
1252 absorption Angstrom exponents ( $AAE$ ) for the study period, cold and warm periods. Mean±  
1253 standard deviation ( $1\sigma$ ), 1st and 3rd Q quartile (25th and 75th percentiles).

Variable	August 2019 - December 2022				cold (November-April)				warm (May-October)			
	mean±sd	median	1 <sup>st</sup> Q	3 <sup>rd</sup> Q	mean±sd	median	1 <sup>st</sup> Q	3 <sup>rd</sup> Q	mean±sd	median	1 <sup>st</sup> Q	3 <sup>rd</sup> Q
$b_{abs}(880)$ ( $Mm^{-1}$ )	0.5±0.9	0.3	0.1	0.6	0.7±0.7	0.5	0.22	0.9	0.4±0.9	0.2	0.09	0,4
$b_{abs}(520)$ ( $Mm^{-1}$ )	0.9±1.6	0.4	0.2	1	1.2±1.2	0.8	0.38	1.5	0.6±1.8	0.3	0.1	0,6
$b_{abs}(370)$ ( $Mm^{-1}$ )	1.2±2.4	0.6	0.3	1.4	1.6±1.6	1.1	0.52	2.1	0.9±2.8	0.4	0.2	0,9
EC ( $ng\ m^{-3}$ )	30±30	20	10	50	50±30	40	20	60	20±30	20	10	30
OC ( $ng\ C\ m^{-3}$ )	459±300	400	300	500	400±200	400	300	500	500±400	400	300	600
* $eBC_{AET}$ ( $ng\ m^{-3}$ )	65±83	36	16	80	84±90	57	25	115	53±158	23	10	45
** $eBC$ ( $ng\ m^{-3}$ )	29±54	13	5	34	44±47	29	12	59	19±57	8.0	4	17
$AAE_{370/950}$	0.96±0.6	0.95	0.7	1.19	0.94±0.4	0.95	0.74	1.1	0.98±0.8	0.95	0.6	1,3
$AAE_{370/520}$	1.0±1.5	0.93	0.4	1.52	0.88±1	0.89	0.49	1.2	1.16±1.9	1.0	0.3	2,0

1254 \*  $eBC_{AET}$  is defined in section 2.2.

1255 \*\*  $eBC$  is defined in section 3.2.

1256